J Mater Sci

Metals & corrosion

Investigation on microstructure and localized corrosion behavior in the stir zone of dissimilar friction-stir-welded AA2024/7075 joint

Chenghang Zhang[1,2,3], Guangjie Huang[1,2,*], Yu Cao[1,2], Qilei Li[1,2], Yulong Zhu[1,2], Xinde Huang[1,2], and Qing Liu[4]

[1] *International Joint Laboratory for Light Alloys (MOE), College of Materials Science and Engineering, Chongqing University, Chongqing 400044, People's Republic of China*

[2] *Shenyang National Laboratory for Materials Science, Chongqing University, Chongqing 400044, People's Republic of China*

[3] *Department of Materials Science and Engineering, KTH Royal Institute of Technology, 100 44 Stockholm, Sweden*

[4] *College of Materials Science and Engineering, Nanjing Tech University, Nanjing 211816, People's Republic of China*

Received: 30 April 2020
Accepted: 10 July 2020

© Springer Science+Business Media, LLC, part of Springer Nature 2020

ABSTRACT

Friction stir welding (FSW) is an effective welding technique to realize the joining of dissimilar aluminum alloys. The microstructural heterogeneities induced by FSW across the joints could have curial implication for the corrosion performance of the joints. In this research, the microstructure and localized corrosion behavior of shoulder interface zone (SIZ), vortex zone (VZ), bottom zone (BZ) and bottom interface zone (BIZ) in the stir zone (SZ) of dissimilar FSW AA2024/AA7075 joint was systematically investigated through detailed microstructural characterization and relevant corrosion tests. The results indicated that plentiful of Cu-rich constituent particles are formed on AA2024 side and the areas near the interface on both sides, and corrosion originates from these regions. Grain size has little influence on corrosion behavior of the SZ, while the local regions with higher stored energy are more sensitive and liable to corrosion. The sequence of mixing degree of materials in the four regions of the SZ is: BZ > VZ > SIZ > BIZ, which is in contrast to the order of corrosion rate. Galvanic corrosion is detected in the SIZ and BIZ, and sufficient mixing of materials significantly weakens the galvanic corrosion, resulting in higher corrosion resistance in the BZ.

Address correspondence to E-mail: gjhuang@cqu.edu.cn

https://doi.org/10.1007/s10853-020-05072-w

Published online: 23 July 2020

Introduction

Currently, in order to lower greenhouse gas emissions, reduce the weight and fuel consumption and optimize the overall performance [1–5], the demand on co-friendly manufacturing processes and lightweight structural material strongly attract the attentions of many researches in the aviation and aerospace industry. Due to high strength-to-weight ratio, aluminum alloys are broadly utilized as a promising alternative for lightweight structures [6, 7]. However, when the conventional fusion welding procedures are employed to join these alloys (e.g., 2xxx and 7xxx series aluminum alloys), there exist some drawbacks/defects, such as segregation, reaction between some reinforcing phases, the formation of coarse microstructure and intermetallic compounds, which are prone to deteriorate the mechanical and corrosion properties of the joints due to the significant difference of thermal expansion coefficients between the solid and the liquid phase [4, 8, 9].

It is widely known that friction stir welding (FSW) can be adopted as an effective solution to improve the low weldability and poor mechanical properties [4, 10, 11]. Nevertheless, corrosion may be a serious issue associated with the application of FSW, particularly for the joining of dissimilar alloys without any protection [12]. This is because the distinctly different metallurgical and microstructural zones are formed due to the asymmetry heat input and mechanical deformation in the joints during FSW [13–17]. The production of conspicuous strip non-uniformity in the weld zone will be most likely to result in the formation of micro-galvanic corrosion cells in the joint, which is unavoidable when involving the welding of dissimilar alloys. Considering that the welded alloys are both conductive and apparently different with respect of corrosion potential, the influence of galvanic coupling between the local zones can be disastrous. Consequently, it is essential to study the influence of the extent of zonal heterogeneities on the localized corrosion behavior in the weld zone of the dissimilar joints.

During FSW, the typical microstructural zones are formed, i.e., stir zone (SZ), thermo-mechanically affected zone (TMAZ), heat-affected zone (HAZ) and base material (BM) [10, 11, 18–20]. It has been reported that the weld area is more susceptible to localized corrosion behavior compared to the BM [21–26]. Lumsden et al. [23] found that the most heavily sensitive region is located at the interface between the nugget zone and the partially recrystallized zone by impregnating the FSW AA7075-T7651 joint in a modified exfoliation corrosion (EXCO) solution. Bousquet et al. [24] studied the corrosion sensitivity of FSW AA2024-T3 joints and pointed out that the HAZ close to the TMAZ is more sensitive to the intergranular corrosion, which results from the presence of intergranular S′(S) phase clusters at grain boundaries. Differently, Paglia et al. [25] reported that higher corrosive attack is located at the interface between the SZ and the TMAZ in their research on the environmental corrosion susceptibility of the FSW AA7050 joints with the addition of scandium. Kang et al. [26] conducted the immersion tests of the FSW AA2024-T3 joints in EXCO solution and verified that the density and degree of the pitting corrosion in the shoulder active zone are slightly larger than those within other regions on the top surface. The initial position of pitting corrosion is between the S phase particles and the adjacent aluminum matrix.

In recent years, due to the increasing demands for multimaterial components, the researches on the corrosion sensitivity of dissimilar FSW joints have been increased. Substantial investigations on the corrosion susceptibilities of friction stir welds were performed in the Al/Mg couples [27], Al/Cu couples [28, 29], Al/brass couples [30], Al/steel couples [31] and dissimilar couples of aluminum alloys [32–41]. Shen et al. [33] investigated the corrosion behavior of the dissimilar FSW AA5083/6082 welds and reported that the corrosion resistance of the dissimilar joints is higher than that of the corresponding BMs. Nevertheless, Fattah-alhosseini et al. [37] studied the electrochemical behavior of dissimilar AA5083/1050 FSW welds and proposed that the passive current density of the FSW joint is in between that of AA1050 and AA5083. Niu et al. [41] identified the influence of BM locations on the corrosion behavior of dissimilar FSW AA2024/7075 joints in an EXCO solution and considered that the corrosion resistance of SZ resembles that of the BM placing in the retreating side (RS). Bertoncello et al. [34] reported the corrosion behavior of dissimilar lap-welded AA7050/2024 joints and concluded that pitting occurs preferentially in the nugget zone of the AA7050 at the open-circuit potential for longer exposures close to the AA7050/AA2024-interface, which can be attributed to the local galvanic coupling. Abreu et al. [35] carried out a multiscale electrochemical research on the corrosion

behavior of the dissimilar FSW AA7475/2024 joints and verified the galvanic coupling by local electrochemical impedance spectroscopy (LEIS) tests, at which the AA7475 acts as anode relative to the AA2024. It is also confirmed a Zn deposit on the intermetallic particles of the AA2024 after 24 h of immersion in the electrolyte. Davoodi et al. [36] studied the corrosion behavior of the dissimilar FSW AA5083/7023 joint. They reported that a galvanic cell is formed at the interfacial region, which is an inhomogeneous borderline consisting of Al–Mg–Zn precipitates. Although the previous studies have reported the corrosion properties of the FSW regions of dissimilar aluminum alloys, very little work has been conducted to ascertain the effect of the zonal heterogeneities on corrosion behavior of the NZ in the dissimilar FSW joints.

Since FSW is an asymmetrical welding process, pronounced zonal heterogeneities (different metallurgical and microstructural zones) are formed during the FSW process of dissimilar materials, inevitably leading to potential difference between different regions of the dissimilar joint, which is likely to have a remarkable influence on the corrosion resistance of the joint. Moreover, there are few reports available to elaborate the localized corrosion behavior in the NZ of the dissimilar FSW AA2024/7075 butt weld. Therefore, we studied the localized corrosion behavior of the SZ in the dissimilar FSW AA2024/7075 joint obtained previously by optimizing the process parameters in the current work. The microstructure of the SZ was characterized through optical microscopy (OM), X-ray diffraction (XRD), scanning electron microscopy equipped with energy dispersive spectroscopy (SEM–EDS), atomic force microscope (AFM), transmission electron microscope (TEM) and electron backscatter diffraction (EBSD). Corrosion behavior was evaluated by immersion tests, weight loss tests, AFM and electrochemical measurements. Vickers hardness test was also carried out. The aim of this work is to clarify the relationship between microstructure and corrosion behavior of the different areas in the SZ of the dissimilar joint.

Experimental procedure

Welding procedure

Sheets of AA2024-T351 (on the advancing side—AS) and AA7075-T651 (on the retreating side—RS) with 6.5 mm thickness were friction stir butt-welded using an FSW machine (FSW-LM-AM16-2D) by employing the H13 hot work steel tool. The FSW tool was positioned equidistant between the two BMs. It is characterized by a concave shoulder diameter of 15 mm, as well as a tapered thread probe with length of 5 mm, tip diameter of 3.76 mm and root diameter of 6.66 mm [7]. Chemical compositions of the two as-received alloys are shown in Table 1. Both plates were cut into 300 mm × 40 mm pieces and welded perpendicular to the rolling direction (RD) by adopting the optimal welding process parameters as proposed in our previous research [42], namely with a rotational speed of 1495 rpm, a traverse speed of 187 mm/min and plunge depth of 0.03 mm. During FSW, the rotation direction of the tool is counterclockwise, and the title angle of the rotating tool is 2.5°. The joint acquired with these process parameters is shown in Fig. 1. After FSW, the thickness of the joint which is not thoroughly welded at the bottom is cut off and the joint with 5 mm thickness is kept to carry the relevant measurements.

Microstructure characterization

The transverse cross section of the dissimilar joint perpendicular to the welding direction (WD) is shown in Fig. 2a, which was cut into four small pieces of samples according to the size. The samples were ground on SiC papers up to 3000 grit and then followed by rough and fine cloth polishing using diamond power slurry. For OM tests, the polished samples were etched with Keller's reagent (HF:HCl:HNO_3:deionized water = 2 mL:3 mL:5 mL:190 mL) for 40 s. The alloy phases were identified by means of X-ray diffractometer (Rigaku D/max 2500PC) using monochromatic Cu$K\alpha$ radiation (λ = 0.1542 nm), with a step size of 0.01° and a time step of 0.1 s. The chemical composition of the samples was analyzed by applying field emission scanning electron microscopy (FESEM, JEOL JSM-7800F) equipped with an energy dispersive spectroscopy (EDS). The corrosion morphology of the samples was characterized by AFM (MFP-3D-BIO).

Table 1 Chemical composition of the aluminum alloys (in wt%)

	Si	Fe	Cu	Mn	Mg	Cr	Zn	Ti	Al
2024-T351	0.05	0.17	4.5	0.6	1.4	0.01	0.03	0.02	Bal.
7075-T651	0.05	0.19	1.7	0.04	2.4	0.2	5.8	0.03	Bal.

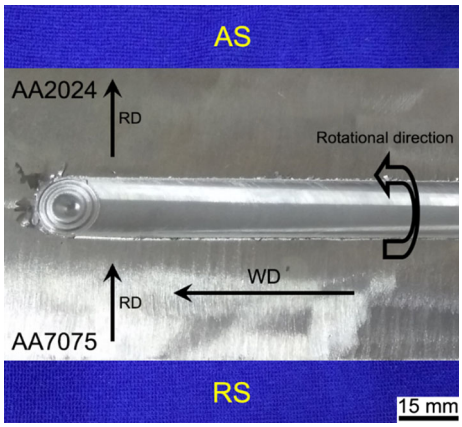

Figure 1 Weld image of dissimilar FSW joint.

The EBSD mapping was conducted on a TESCAN MIRA3 SEM equipped with a HKL-EBSD system with a step size of 0.3 μm to reveal the grain structure. Before EBSD, the polished samples were electropolished in an electrolyte of 10 vol% perchloric acid plus 90 vol% ethanol at 2–5 °C and 15 V for 100 s. The Channel 5 software was employed to conduct the EBSD data analysis. TEM specimens of the BMs and the welded zone of joint were prepared in a 25% HNO_3 methanol solution at − 30 °C using the twin-jet electropolishing technique. The TEM specimen at the interface of the SZ was prepared by employing focused ion mill (FIB, Zeiss AURIGA) technique. The precipitates were investigated by using TEM (FEI TECNAI G2 F20) equipment, operated at 200 kV.

Hardness measurement

Vickers microhardness tests were conducted using Vickers hardness tester (MH-5L). The hardness profile for each specimen was performed along the cross section of the joint perpendicular to the WD using a load of 200 gf and a dwell time of 10 s. The distance between each indentation is set to 0.1 mm.

Corrosion tests

Corrosion behavior of the samples acquired from different positions in the SZ was studied via immersion test, PDP and EIS tests. Immersion tests were carried out in naturally aerated 3.5% NaCl solution for 12 h, 69 h, 192 h and 336 h. The weight loss test was conducted after immersion of 336 h to evaluate the corrosion rate. The experimental process and the calculation method have been described in our early work [42].

Electrochemical tests were carried out by electrochemical system (Gamry, Germany) in 3.5 wt% NaCl aqueous solution at room temperature. The SZ was cut into the four samples and their dimensions are shown in Fig. 2a. Prior to the electrochemical tests, the side and back of the specimens after cutting were coated by insulating epoxy resin so that the surface to be tested was only exposed to the solution. The experiments were conducted with a three-electrode cell configuration consisting of the studied samples from different zones in the SZ as the working electrode, a platinum sheet as counter electrode and a saturated calomel electrode (SCE) as reference electrode. The PDP test was conducted from − 1600 mV to + 200 mV at a scan speed of 1 mV s^{-1}. Tafel-type fitting of the data was employed to determine the corrosion potential (E_{corr}) and corrosion current density (I_{corr}) from the polarization curves. The EIS test was carried out in the potentiostatic mode by applying a sinusoidal voltage with an amplitude of 10 mV and frequency from 100000 to 0.01 Hz. The ZSimpWin software was used to analyze of the EIS data. To ensure the accuracy of experimental data, these above electrochemical tests were conducted separately and repeated at least for three times in order to collect three reliable test results.

Results and discussion

The backscatter electron (BSE) images at the cross section of different zones in the SZ of the dissimilar FSW joint are exhibited in Fig. 2a. It is clearly observed that the primary material flow trend is from AS (AA2024) to RS (AA7075) under the action of the tool shoulder and the tool pin. Four distinct regions can be seen as shown in Fig. 2b–e, namely (1)

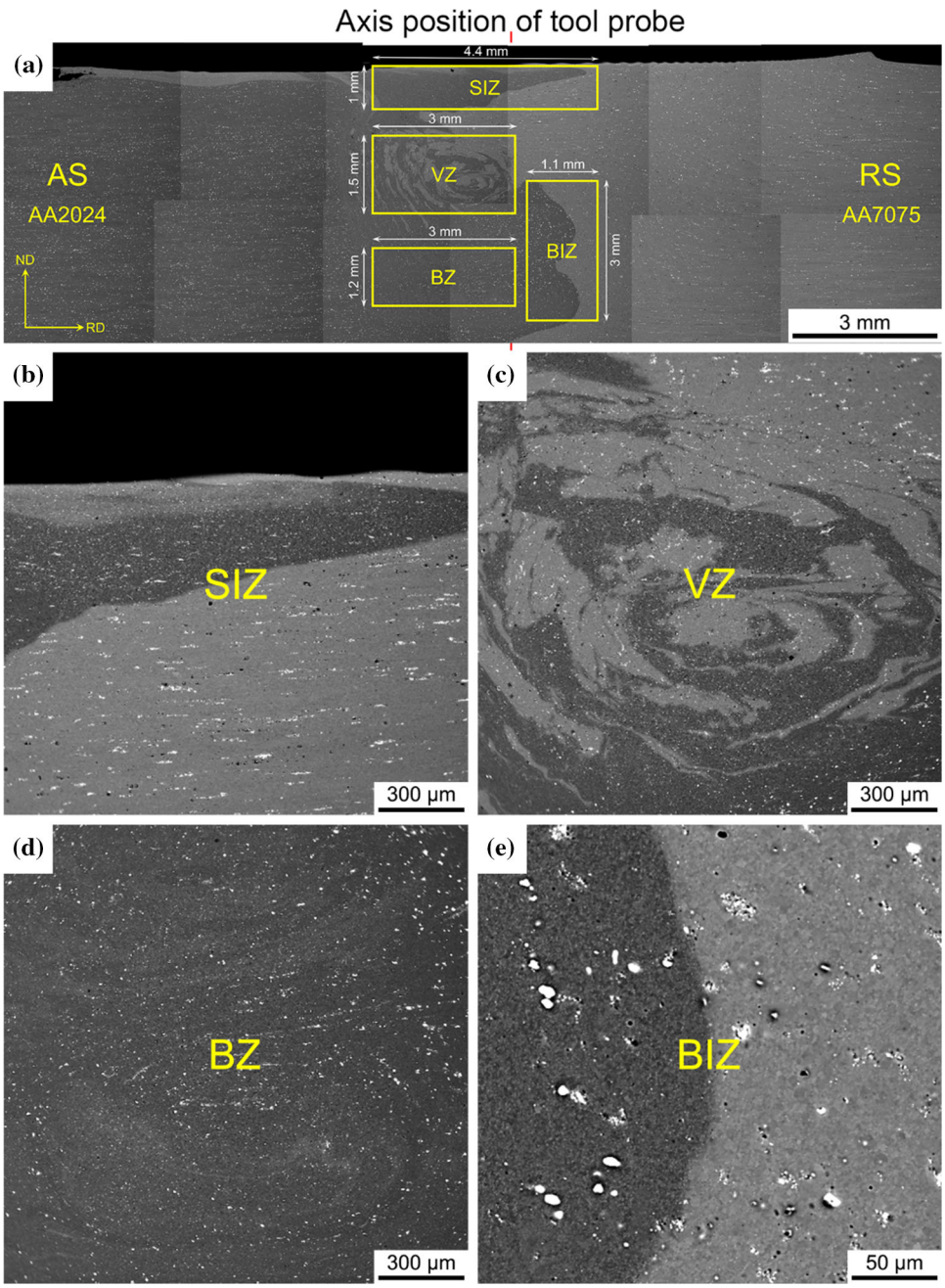

Figure 2 BSE images showing the studied regions in the SZ of the dissimilar FSW joint: **a** BSE images jigsaw of the weld, **b** SIZ, **c** VZ, **d** BZ and **e** BIZ.

shoulder interface zone (SIZ), (2) vortex zone (VZ), (3) bottom zone (BZ) and (4) bottom interface zone (BIZ). The SIZ demonstrates the migration of materials from AS (AA2024) under the rotational friction extrusion of the tool shoulder [43]. The VZ is featured by some typical onion ring structures as a result of the mixing of the two BMs [44–46], which is located below the tool shoulder and at the root of the tool pin. The BZ is only affected by the tip of tool pin. The BIZ is near the borderline of material flowing from AS to RS. Since the different regions in the SZ are subjected to various degrees of heating and plastic deformation during FSW, some complex zonal heterogeneities are generated. The zonal inhomogeneity becomes even more complex in the weld areas when involving dissimilar alloys, thereby affecting the mechanical and corrosion properties of the joint. In order to clarify the local corrosion behavior due to the zonal heterogeneities during the dissimilar FSW welds of AA2024-T351 and AA7075-T651, the above four regions were studied in detail.

Phase analysis

X-ray diffraction analysis

The purpose of XRD analysis is to detect the formation of various phases in the alloys. Thus, XRD analysis was executed on each specimen at the different positions of the dissimilar joint, as shown in Fig. 3. Due to the positions close to those in the diffraction pattern of the pure Al power, the sharp and strong peaks are derived from Al matrix. The intensity of Al peaks is higher due to larger percentage of Al matrix at the BMs and the weld zone. It is worth noting that the smaller diffraction angle regions were magnified to present the low-intensity peaks. As illustrated in XRD patterns, it can be obviously seen that Al_2Cu and $MgZn_2$ can be detected in the AA2024 and AA7075, respectively. In addition, some constituent particles, such as Al_2CuMg, AlCuMg and Al_7Cu_2Fe, can be found in AA2024, while Al_7Cu_2Fe presents in AA7075. The four samples in the SZ present similar XRD patterns because they all contain two BMs (Fig. 2b–e). Accordingly, the above-mentioned constituent particles all exist in these four regions. Interestingly, the diffraction peak intensity of VZ and BZ is lower than that of SIZ and BIZ (the black ellipse in Fig. 3). This could be because the original constituent particles in BMs are broken or dissolved in the VZ and BZ during material mixing under the action of the stirring tool, which weakens the intensity of diffraction peaks to a certain extent.

SEM/EDS characterization

Figure 4 shows the SEM images of the two BMs and the four regions in the SZ, and the EDS analysis results are summarized in Table 2. Bulk EDS spectrum analyses indicate that the chemical compositions of the two BMs conform to the results of XRD patterns (Fig. 3). An inhomogeneity microstructure with intermetallic particles usually exist in aluminum alloys. Some constituent particles of Al–Cu–Mg, Al–Cu–Fe–Mn and Al–Cu–Fe types are distributed in the AA2024 BM (Fig. 4a), and the Al–Cu–Fe-, Al–Zn–Cu–Fe- and Al–Zn–Cu–Mg–Fe-type particles can be found in the AA7075 BM (Fig. 4b). The precious research has shown that the uneven distribution of Cu-rich particles in AA2024 can be regarded as the dominant factor of pitting and stress corrosion cracking [47]. The corrosion resistance of AA7075 is weak because of the large amount of second phase intermetallic particles which may be anodic or cathodic relative to the alloy matrix [36].

Through bulk EDS analysis (Table 2), the intermetallic particles with various sizes and types near the interfacial regions are illustrated in Fig. 4c, f, which are proved to be Al–Cu–Mg (Al_2CuMg) and Al–Zn–Cu–Mg–Fe particles at the interface of SIZ and BIZ. In addition, Al–Zn–Cu–Fe and Al–Cu–Fe–Mn particles are found in the BIZ. The interfacial region is a combination of intermetallic phases of the two BMs and its chemical composition can be changed due to the diffusion and migration of alloying elements from adjacent substrates during FSW. The sharp

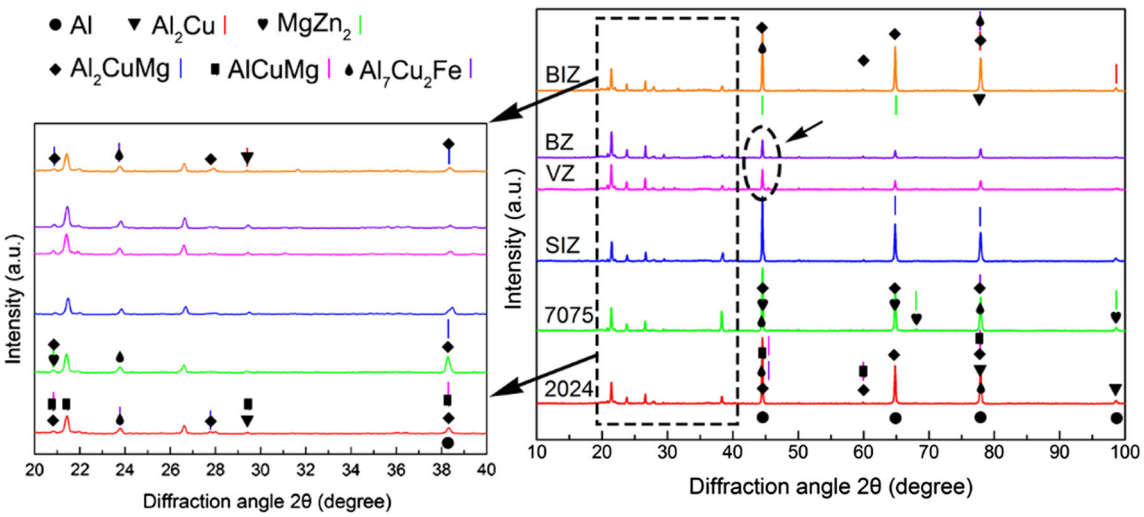

Figure 3 XRD patterns of the two BMs and the four regions in the SZ (reference codes: Al: 04-0787, Al_2Cu: 25-0012, $MgZn_2$: 34-0457, Al_2CuMg: 28-0014, AlCuMg: 28-0015, Al_7Cu_2Fe: 25-1121).

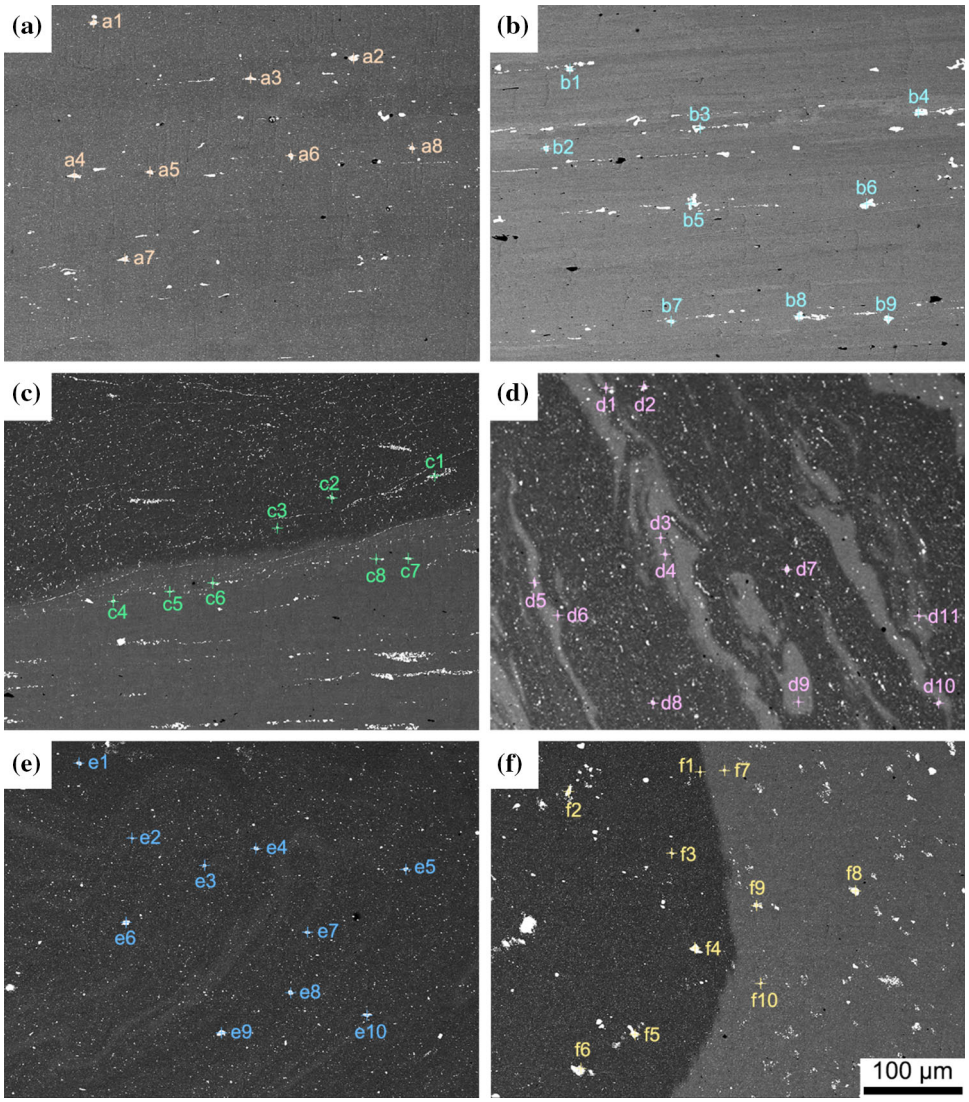

Figure 4 SEM images of the two BMs and the four regions in the SZ: **a** 2024 BM, **b** 7075 BM, **c** SIZ, **d** VZ, **e** BZ and **f** BIZ.

concentration gradient within the interfacial area may result in the formation of galvanic cells that provide the driving force for corrosion.

According to the EDS analysis results in Table 2, Al–Zn–Cu–Fe-, Al–Zn–Cu–Mg-, Al–Zn–Cu–Mg–Fe- and Al–Zn–Cu–Mg–Fe–Mn-type particles can be observed in the VZ and BZ. Basically, almost all particles in the VZ and BZ contain Zn element, which can be ascribed to the flow behavior of welding materials. During FSW, the elements in the two BMs diffuse into each other when materials mix. Due to Zn element only existing in the AA7075 BM, it can be used as a feature marker element to analyze the mixing degree of material flow. Compared to the SIZ (Fig. 4c) and BIZ (Fig. 4f), it can be seen that both VZ (Fig. 4d) and BZ (Fig. 4e) exhibit some apparent mixed flow traces, indicating a better mixing of materials at a macroscopic level since the proportion of materials not properly mixed is smaller than that of the SIZ and BIZ.

In order to get an intuitional observation about elements distribution across the four regions in the SZ, the EDS mappings are presented in Fig. 5, showing the distribution of various elements with different colors. An obvious district distribution of different elements, especially Zn, Cu and Mg, can be observed within these four regions. According to the chemical constituents of the two BMs in Table 1, Cu mainly presents in AA2024, while AA7075 principally contains Zn. Besides, the mass fraction of Mg in AA7075 is higher than that in AA2024. Therefore, mixing traces of material flow during FSW are clearly observed as a function of elements mapping distribution. There is a clear demarcation line on both sides

Table 2 Concentrations of elements acquired by EDS analysis (at%) results of the two BMs and the four regions in the SZ (SEM images in Fig. 4)

		2024		7075		SIZ			VZ		BZ		BIZ
Location	Al	Zn	Cu	Mg	Fe	Mn	Location	Al	Zn	Cu	Mg	Fe	Mn
a1	48.2	-	25.6	26.2	-	-	d4	73.6	2.1	4.6	-	19.7	-
a2	67.6	-	18.8	-	9.0	4.6	d5	83.2	2.8	2.2	3.1	8.7	-
a3	74.9	-	15.9	-	7.5	1.7	d6	93.7	1.5	2.1	2.7	-	-
a4	68.4	-	21.2	-	10.4	-	d7	49.3	1.0	24.9	24.8	-	-
a5	66.4	-	21.2	-	9.7	2.7	d8	70.8	0.9	18.3	-	7.9	2.1
a6	48.5	-	25.6	25.9	-	-	d9	84.6	3.0	2.0	2.9	7.4	-
a7	65.8	-	21.2	-	10.3	2.7	d10	77.2	1.7	4.9	1.3	14.9	-
a8	48.6	-	25.5	25.9	-	-	d11	83.8	2.6	2.6	2.6	8.4	-
b1	83.9	2.7	2.5	-	10.9	-	e1	47.0	1.1	26.0	25.9	-	-
b2	67.0	1.4	5.0	1.5	25.1	-	e2	67.6	1.4	29.7	1.3	-	-
b3	74.7	2.3	4.3	-	18.7	-	e3	64.1	1.5	33.1	1.3	-	-
b4	77.9	1.2	3.9	-	17.0	-	e4	46.1	1.2	26.4	26.3	-	-
b5	73.4	2.1	4.5	-	20.0	-	e5	47.0	1.1	26.1	25.8	-	-
b6	69.2	-	5.7	-	25.1	-	e6	47.7	0.8	25.7	25.8	-	-
b7	46.0	2.4	25.1	26.5	-	-	e7	49.9	1.0	24.3	24.8	-	-
b8	88.6	2.9	1.5	3.0	4.0	-	e8	49.4	1.2	24.6	24.8	-	-
b9	73.2	2.3	4.7	-	19.8	-	e9	47.4	1.1	25.6	25.9	-	-
c1	94.4	-	3.8	1.8	-	-	e10	54.2	1.0	22.2	22.6	-	-
c2	86.3	0.6	8.1	1.7	3.3		f1	71.2	-	15.3	13.5	-	-
c3	95.4	-	2.2	2.4	-	-	f2	69.1	-	22.0	-	8.9	-
c4	74.4	2.3	4.3	18.1	0.9	-	f3	48.4	-	25.8	25.8	-	-
c5	75.1	2.2	4.1	1.2	17.4	-	f4	48.5	-	25.6	25.9	-	-
c6	72.8	2.4	5.1	1.0	18.7	-	f5	67.3	-	20.7	-	10.0	2.0
c7	77.8	2.5	3.4	1.6	14.7	-	f6	65.4	-	21.3	-	9.3	4.0
c8	73.9	2.5	4.1	1.0	18.5	-	f7	58.7	2.6	18.6	20.1	-	-
d1	83.1	2.4	2.8	2.2	9.5	-	f8	73.1	2.1	4.3	-	20.5	-
d2	47.5	1.2	25.9	25.4	-	-	f9	73.6	2.1	4.8	-	19.5	-
d3	81.8	2.5	2.7	2.1	10.9	-	f10	73.9	2.1	5.0	-	19.0	-

of the interface in the SIZ and BIZ. On the basis of the results in Figs. 2 and 5, the order of mixing degree of material flow in the four regions can be concluded: BZ > VZ > SIZ and BIZ.

The EDS line scan results of Zn, Cu and Mg elements around the interface within the four regions are illustrated in Fig. 6. To ensure the accuracy of interface element analysis, the line scan was performed twice for each area. An obvious transition behavior can be clearly seen at the interface of SIZ and BIZ, showing the diffusion of Zn, Cu and Mg at the interface as depicted in Fig. 5. It is worth noting that the diffusion distance of the Zn, Cu and Mg at the interface of SIZ is greater than that of the BIZ. This is because they experience different thermal cycles during FSW. The diffusion distance depends on temperature and time, which can be expressed as follows [48]:

$$X^2 = 6Dt \tag{1}$$

$$D = D_0 \exp\left(-\frac{E}{RT}\right) \tag{2}$$

where X is the diffusion distance, D is the diffusion coefficient, t is the time, D_0 is a material constant, E is the activation energy, T is the temperature and R is the gas constant. The peak temperature of SIZ at the top is higher than that of BIZ at the bottom [49]. Based on Eqs. (1) and (2), it can be inferred that higher peak temperature is prone to increase diffusion rate, leading to higher mixing degree of material flow. Accordingly, it is believed that the mixing degree of SIZ is higher than that of BIZ. Besides,

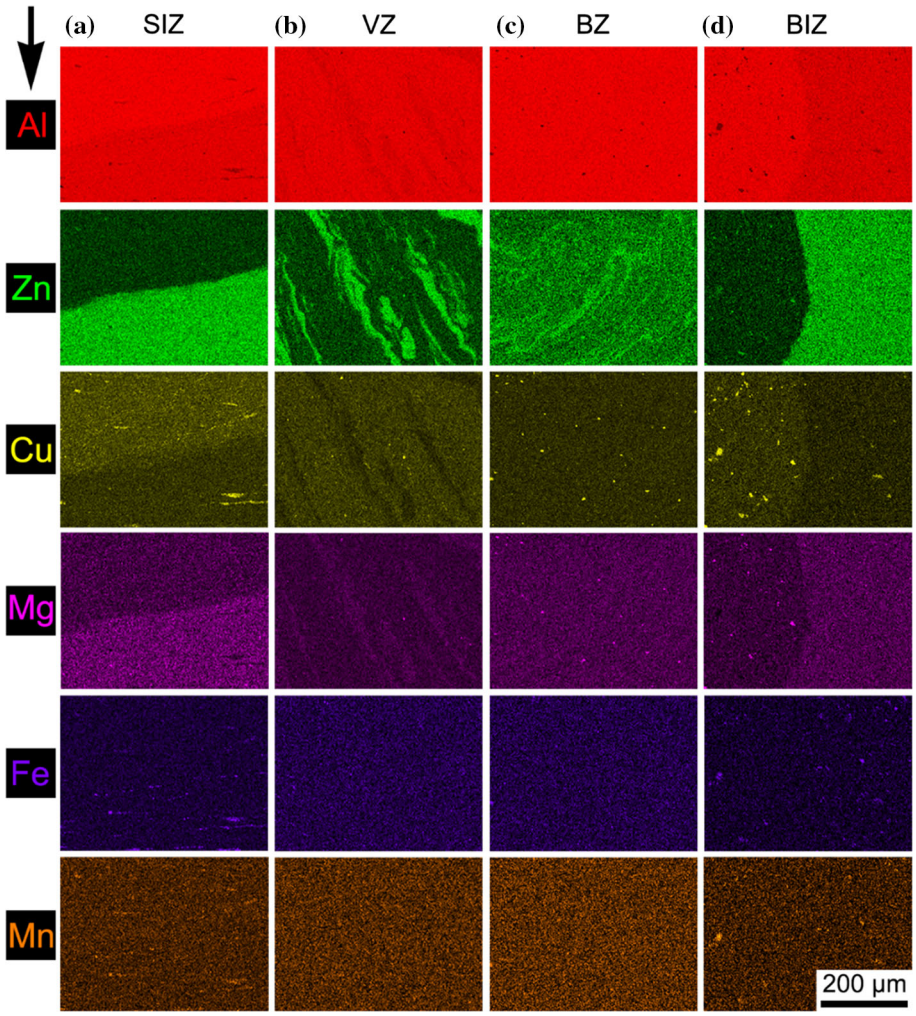

Figure 5 Element distribution mapping of the four regions: **a** SIZ, **b** VZ, **c** BZ and **d** BIZ.

Figs. 5 and 6 show that the distribution of Zn, Cu and Mg elements in the VZ presents a sharply fluctuant pattern, indicating an inferior mixing degree compared with that of BZ. Thus, we can conclude from the results in Figs. 2, 5 and 6 that the order of mixing degree of material flow in the four regions is: BZ > VZ > SIZ > BIZ.

TEM/EDS analysis

The thin-foil specimen at the interface of BIZ extracted by FIB technique is shown in Fig. 7a. The pink square area was enlarged and is shown in Fig. 7b, which displays the distribution of second phases and their corresponding element distribution mappings. It is observed that Al–Cu–Mg-type and Mn-rich-type particles with a larger size are mainly distributed at the interface of BIZ. Besides, Cu, Mg and Mn elements are evenly distributed, while a clear boundary can be detected from the distribution mapping of Zn element. The line scan EDS results of Zn element at the interface in Fig. 7c, d also demonstrate a conspicuous transition behavior (the blue ellipse in Fig. 7c, d), indicating a significant diffusion behavior at a more microscopic scale when materials flow and mix during FSW.

For AA2024 alloy, the general precipitates sequence from the supersaturated solid solution (SSSS) → Guinier–Preston–Bagaryatsky (GPB) zones → S''/GPB2 → S' → S [50]. The structure of the S' phase is the same as that of the equilibrium S phase, but they have different lattice dimensions. The bright-field TEM images of the 2024-T351 BM are shown in Fig. 8a, b, in which two different types of particles can be found. One is the deep contrast long-rod-shaped particle with the length of 0.5–1 μm. The other is the shallow contrast short-rod-like particle, which can be identified as Ω phase with the chemical

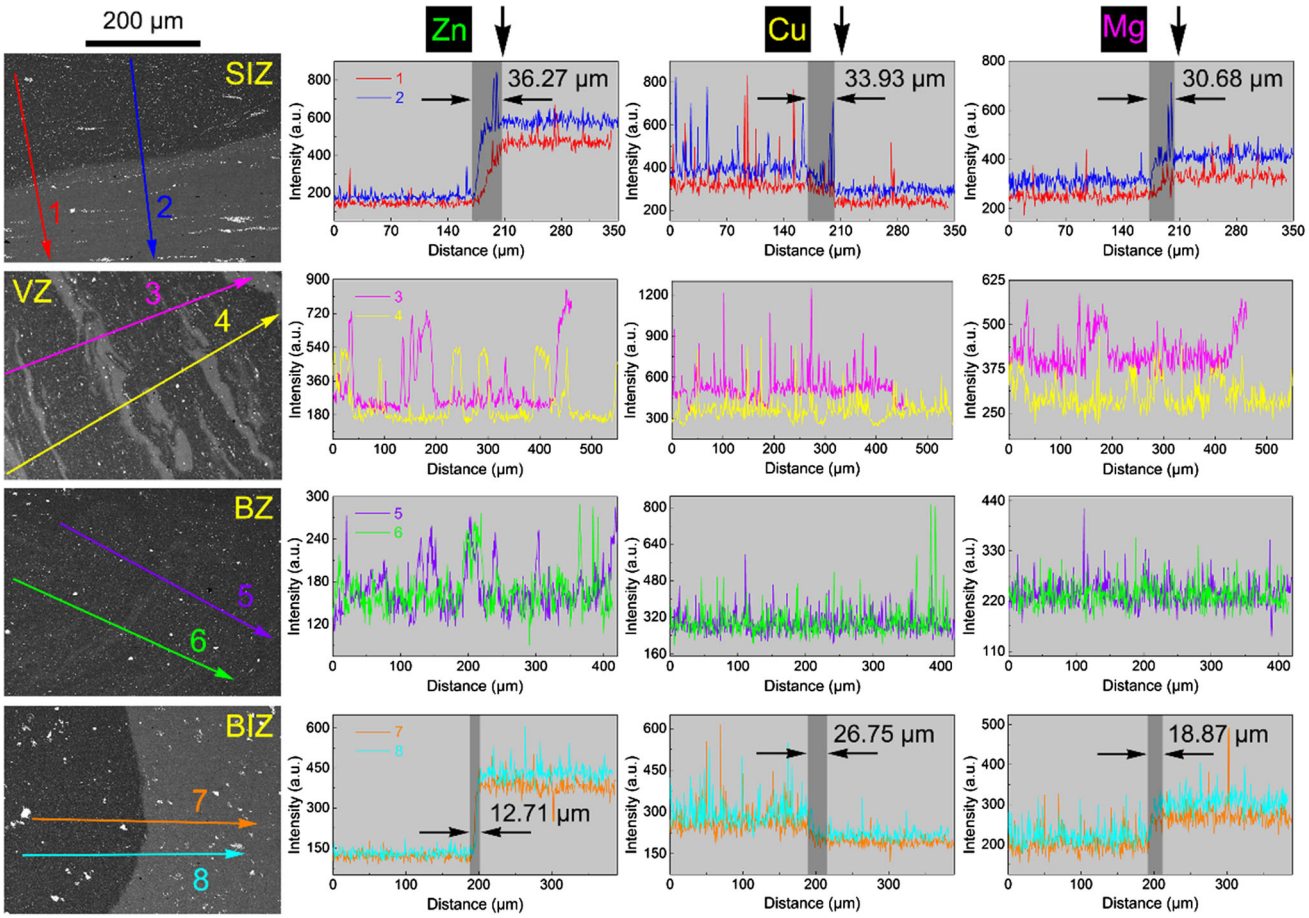

Figure 6 Linear EDS analysis results in the SIZ, VZ, BZ and BIZ.

composition of $Al_{20}Cu_2Mn_3$ and nanometer precipitated S phase with the chemical composition of Al_2CuMg [51]. The TEM image within Zn-depleted region is displayed in Fig. 8c, which can be subdivided into different parts with a higher magnification as depicted in Fig. 8d–f. According to the EDS results in Table 3, it is found that many fine second phases such as Al–Cu–Mg, Al–Cu–Mn and Al–Cu–Mg–Mn particles are homogeneously distributed in the Zn-depleted regions of the interface in the BIZ. Their sizes and element compositions are disparate from AA2024 BM. This is because the second phase particles existing in the two BMs are broken and then re-precipitate due to the thermal cycle and deformation under the agitation of the tool during FSW.

For 7xxx series alloys, the precipitation sequence is generally accepted as solid solution → GPB zones → η' phase (rod) → η phase (disk) [52]. The η' and η phases are the semi-coherent metastable and equilibrium $MgZn_2$ phase, respectively, and both of them have a hexagonal crystallographic structure [53]. The AA7075-T651 used in this study is mostly strengthened by precipitates. Figure 9a, b exhibits the bright-field TEM images of 7075 BM. The microstructure of 7075 BM consists of η' and η precipitates, which are uniformly distributed within the matrix and along the grain boundaries. Figure 9c shows the TEM images of Zn-rich side in Fig. 7b. Figure 9d–f shows the enlarged TEM images in Fig. 9c. The EDS analysis data in Table 4 show that Al–Zn–Cu–Mg–Fe-, Al–Zn–Cu–Mg–Mn-, Al–Zn–Cu–Mg-, Al–Cu–Mg–Mn-, Al–Cu–Mg- and Al–Cu–Mn-type particles with nanoscale are formed in the Zn-rich side of the interface in the BIZ.

The formation of these nanometric particles at the interface (Figs. 8, 9) largely depends upon the atomic diffusion at the interface, which is driven by the temperature during FSW. Accordingly, temperature is the most important factor that affects the diffusion coefficient [54–56]. According to Eq. (2), the higher the temperature, the faster the diffusion rate. Thus, the precipitation rate of the second phase increases

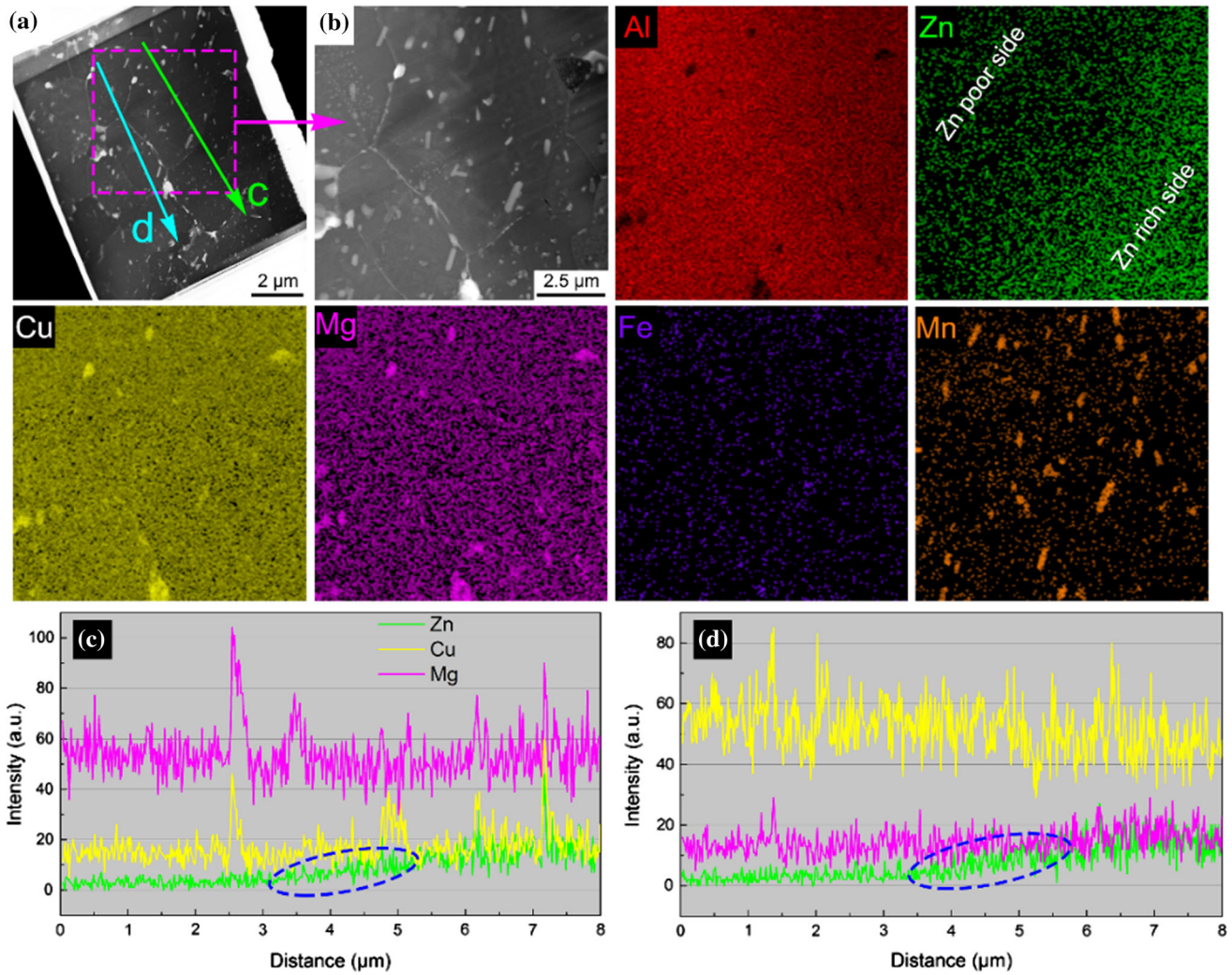

Figure 7 Different views for TEM analysis: **a** thin-foil sample extraction by FIB technique, **b** enlarged view and the corresponding mapping scan EDS results, **c**, **d** line scan EDS results.

with the temperature increases. The growth tine of the second phase is limited during FSW, which results in insufficient time to grow, forming nanometric intermetallic compounds. Gotawala and Shrivastava [57] developed a numerical mode consisting of Fick's second law-based diffusion model in conjunction with a thermo-mechanical model, which shows the significance of the atomic diffusion at the weld interface, toward the precipitated phases formation.

Figure 10 shows the TEM images of the BZ. Figure 10a, b shows that a large number of fine precipitate particles with the sizes less than 300 nm are homogeneously distributed in the grain interior and at the boundaries. Based on the difference of various morphologies in Fig. 10c–e, the precipitate particles can be divided into three kinds of shapes: irregular shape, rod-like and discoid shape, which are, respectively, identified to be AlCuMg (Fig. 10c), $Al_{11}Cu_5Mn_3$ (Fig. 10d) and Al_6CuMg_4 (Fig. 10e) phases by selected area electron diffraction (SAED).

Grain structure investigation

The corrosion behavior can be affected by the grain size and its distribution in polycrystalline materials [58, 59]. Thus, we conducted some EBSD tests on the two BMs and the four regions in the SZ of the dissimilar joint to investigate the grain structure. As shown in Fig. 11a, b, the elongated grains of the two BMs arising from the rolling process are very long and the grain width of AA2024 BM is wider than that

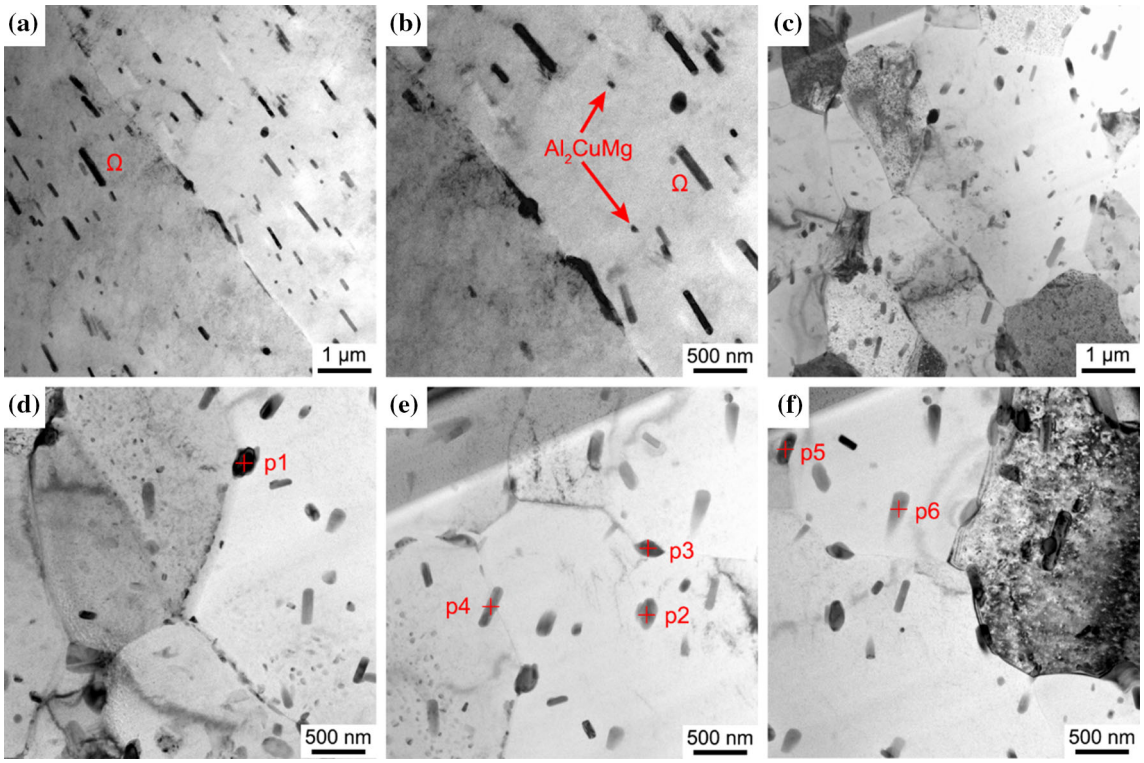

Figure 8 TEM images of precipitates in **a**, **b** 2024 BM, **c**–**f** Zn-poor regions corresponding to Figure 7b.

Table 3 Concentrations of elements acquired by EDS/TEM analysis (at%) in Zn-depleted regions of Fig. 7b (TEM images in Fig. 8d–f)

Locations	Al	Zn	Cu	Mg	Fe	Mn
p1	56.58	0.31	22.15	20.86	0.09	0.01
p2	61.74	0.19	20.34	17.67	0.01	0.04
p3	50.93	0.30	26.21	22.50	0.06	0.00
p4	89.63	0.13	4.39	0.82	0.08	4.95
p5	84.78	0.13	5.66	0.71	0.14	8.58
p6	87.71	0.17	4.59	1.36	0.16	5.02

of AA7075 BM. However, the microstructure in the SZ is characterized by the fine and equiaxed recrystallized grains (Figs. 11c–f, 12) resulting from the severe plastic deformation and thermal exposure during FSW. The grains experience severe deformation, which produces abundant dislocation substructures. Then the friction heat can stimulate these substructures into recovery and recrystallization. A large number of nucleation sites can be generated during cooling. Consequently, the grains are refined and the number of grain boundaries is increased. In addition, it is observed that the grain size on both sides of the interface is different, which presents evident interface (Fig. 11c, f) and banded distribution (Fig. 11d) characterization. The grain structure of the BZ (Fig. 11e) is more homogeneous than that of other three regions (SIZ, VZ and BIZ, Fig. 11c, d, f), which indicates that more homogeneous mixing occurs in the BZ.

The local misorientation maps of the four regions in the SZ are illustrated in Fig. 13. Focused on the analysis point in the 3 × 3 grid, the average value of the misorientation between the point and the neighboring eight points is calculated as the local misorientation value of the center point, and the local misorientation of more than 2° is discarded. In addition, the dislocation density can be calculated by using the local misorientation θ_{loc} [60, 61]:

$$\rho = \frac{\alpha\theta_{\mathrm{loc}}}{ndb} \tag{3}$$

in which α is the grain boundary type parameters, b is the Burgers vector, n is the defined area size and d is the step size of EBSD measurements. Therefore, the stored energy E can be obtained by the following formula:

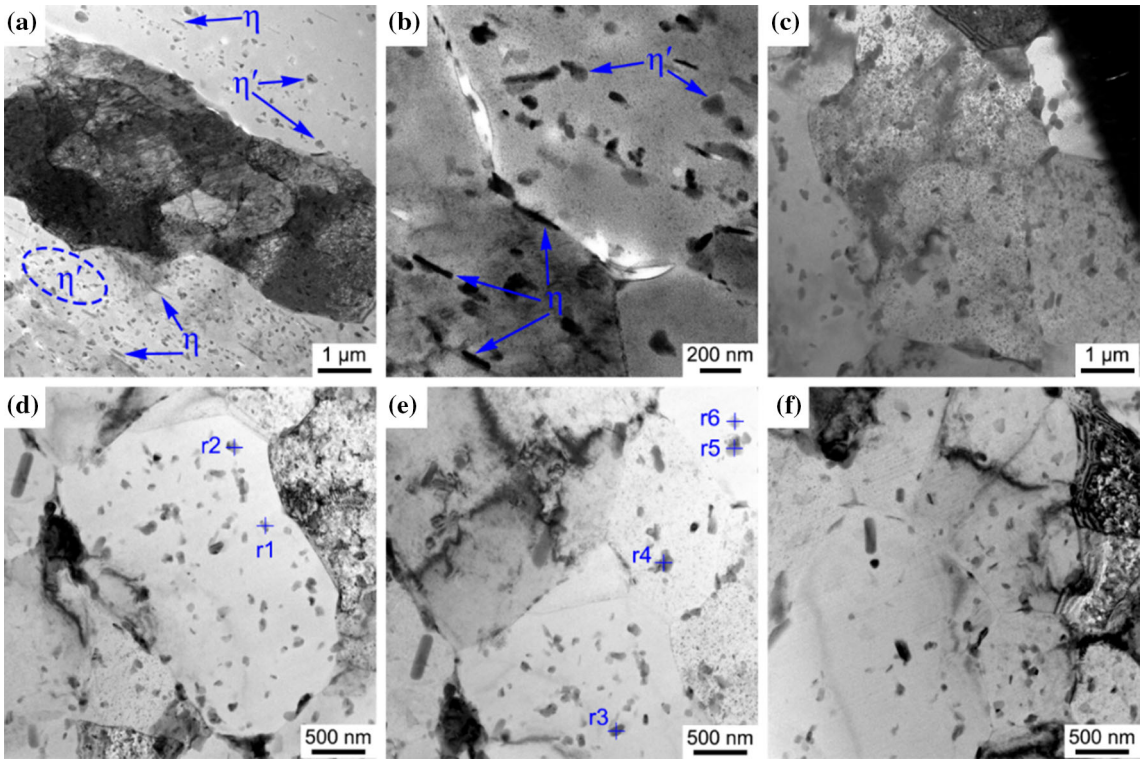

Figure 9 TEM observations of the distribution of precipitates in **a**, **b** 7075 BM, **c**, **f** TEM images of Zn-rich sides in Figure 7b.

Table 4 Concentrations of elements acquired by EDS/TEM analysis (at%) in Zn-rich areas of Fig. 7b (TEM images in Fig. 9d–f)

Locations	Al	Zn	Cu	Mg	Fe	Mn
r1	87.71	0.55	4.62	1.36	0.14	5.62
r2	89.66	1.58	2.85	3.12	2.22	0.56
r3	86.38	1.33	4.36	2.83	0.28	4.82
r4	82.72	0.77	6.64	0.70	0.12	9.04
r5	72.59	5.18	4.70	17.40	0.03	0.10
r6	91.68	0.31	22.15	20.86	0.09	0.01

$$E = \frac{1}{2}\rho\mu b^2 = \frac{5}{6}\alpha\mu\theta_{\mathrm{loc}} b \tag{4}$$

where μ is the shear modulus. Thus, the stored energy is proportional to the local misorientation. As shown in Fig. 13, the heterogeneous distribution of the local misorientation resulting from the lattice distortion during plastic deformation demonstrates the existence of stored energy, which presents a district difference in the stored energy on both sides of the interface in the SIZ and BIZ. After calculation by using Eq. (4), the stored energy on the 2024 and 7075 side (of the SIZ and BIZ) is about 44.1 and 18.9 kJ/m^3, respectively. This implies that the stored energy on the 2024 side is significantly higher than that of on the 7075 side. The rotation direction of the FSW tool is from AS (AA2024) to RS (AA7075), which causes higher deformation occurring on the 2024 side in the SZ, finally resulting in higher local misorientation on the 2024 side. Besides, the stored energy in the VZ and BZ is relatively lower than that in the SIZ and BIZ due to the sufficient mixing of materials in the VZ and BZ.

Hardness tests

Figure 14 displays the hardness indentation of the BMs and illustrates that the measured average hardness values of AA2024 is approximately 20 HV lower than that of AA7075. As shown in Fig. 15, the dark and the light color zones are corresponding to the matrix of AA2024 and AA7075, respectively. The direction of the blue arrow is the order of hardness indentation value from left to right in hardness profile. It can be observed that the hardness values of the four regions are lower than the corresponding BM. The previous researches by Ma et al. [62] and Cam

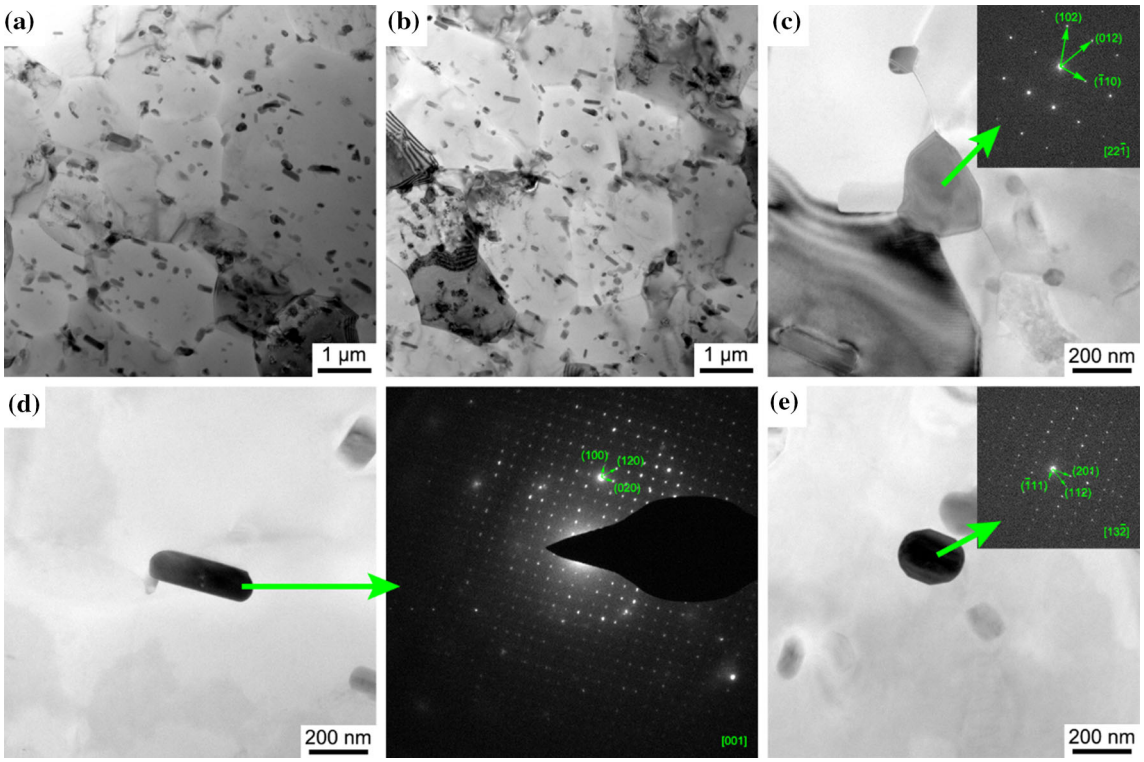

Figure 10 TEM images of the precipitates in BZ: **a**, **b** low-magnification images, **c**–**e** high-resolution images and the corresponding diffraction spots: **c** AlCuMg, **d** $Al_{11}Cu_5Mn_3$ and **e** Al_6CuMg_4.

et al. [63] proposed that the FSW of precipitation-hardened aluminum alloys results in lower hardness values in the weld regions due to the dissolution and coarsening of strengthening precipitates during FSW. In addition, Fig. 15a–c, j–l shows that the hardness value at the interface of SIZ and BIZ is between those values of the materials on both sides. Such a distinct gradient effect in hardness value at the interface could be attributed to the apparent diffusion behavior of the elements on both sides of the interface under the stirring action of the tool (Figs. 5, 6). Moreover, the hardness profile in the VZ reveals a trend of fluctuation (Fig. 15f). This is because the two BMs are mixed and then alternately distributed under the stirring process (Figs. 5, 6), forming the banded structure in Fig. 15d, e. There is almost no significant variation in the hardness profile of the BZ due to sufficient mixing of materials (Fig. 15g–i).

Corrosion testing

Corrosion morphologies

Figure 16 displays the surface corrosion morphologies of the BMs and the four regions in the SZ in 3.5 wt% NaCl solution after immersion of 12 h. Clearly, slight pitting occurs in the two BMs (Fig. 16a, b), while a large number of pitting holes are found in the SZ (Fig. 16c–f). Besides, the pitting areas are mainly concentrated in the SZ near the AS derived from AA2024 BM. The dark and the light areas in Fig. 16c, d, f represent the matrix of AA2024 BM and AA7075 BM, respectively. The number and density of the pitting holes on both sides of the interface line in the SIZ (Fig. 16c) and BIZ (Fig. 16f) are totally different, and more pitting holes can be found on the side of AA2024 BM. The corrosion in the VZ is not uniform, which results from the uneven flow behavior of materials, and a large number of pits are mainly concentrated in the AA2024 BM. Furthermore, there are only a few pits between the layers in the VZ as indicated with the red ellipse in Fig. 16d. The pitting in the BZ is uniformly distributed (Fig. 16e) due to the sufficient material mixing. The above pitting corrosion mainly occurs in the welded zone related to AA2024 BM. According to the EDS analysis results in Fig. 4 and Table 2, the Cu element exists throughout the SZ, which is prone to deteriorate the corrosion performance of Al alloys through

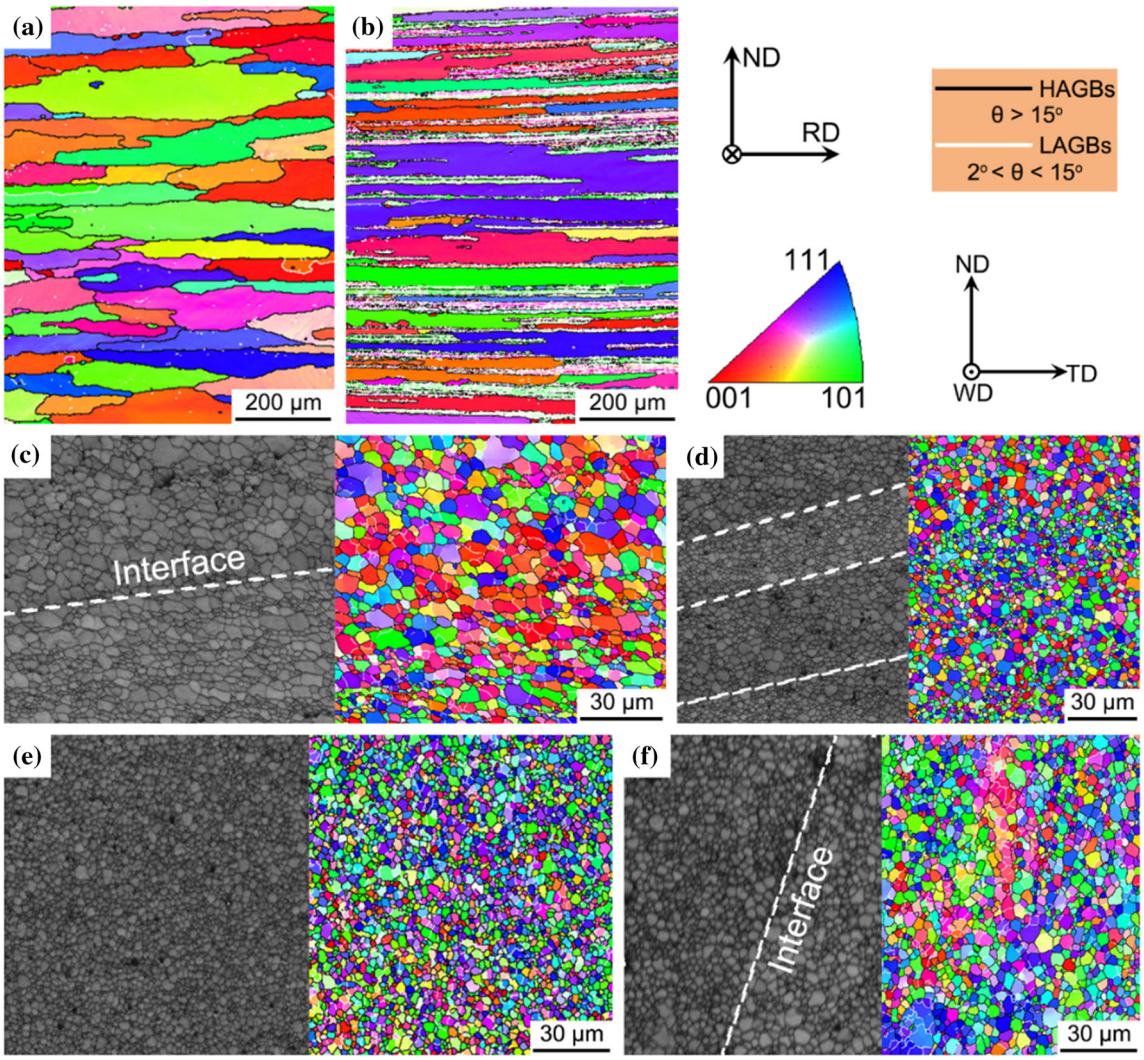

Figure 11 EBSD maps of the two BMs: **a** AA2024 BM, **b** AA7075 BM, **c** SIZ, **d** VZ, **e** BZ and **f** BIZ.

the formation of a galvanic cell in the matrix [64]. The corrosion of materials mainly depends on the surface passivation film. A homogeneous passive film can be formed due to the fact that aluminum alloy has a large affinity for oxygen. This film is liable to prevent Cl^- from corrosion medium. With the increase in the immersion time, a large number of Cl^- accumulate on the surface of passive film and then penetrate into the Al matrix by means of the infirm point. Finally, the pitting nuclei can be produced by the combination of Cl^- and position ions of the Al matrix.

As shown in Fig. 17, some larger pits related to the activities of constituent particles can be observed on the exposed surface of the two BMs after immersion for 69 h. In addition, it is found that some attacked spots in AA2024 BM, termed as corrosion rings, are surrounded by circular areas with little or no trace of attack as marked with the blue ellipse in Fig. 17. The corrosion rings are cathodically protected by the anodic reactions occurring at the center of the pits. The same corrosion behavior has also been found in AA2198 alloy, regarded as a typical characteristic of localized corrosion [65]. With immersion time up to 192 h, the size of corrosion rings increases markedly, leading to an intersection between some adjacent rings. For the AA7075 BM, the number, density and size of local corrosion pits increase with increasing the immersion time. In the welding zones, slightly larger corrosion pits begin to appear at the interface of the SIZ and BIZ. Between layers in the VZ and BZ, the larger corrosion pits also appear. After 336 h of immersion, the corrosion attack of the four regions in the SZ becomes more and more serious with the extension of immersion time. By comparing the

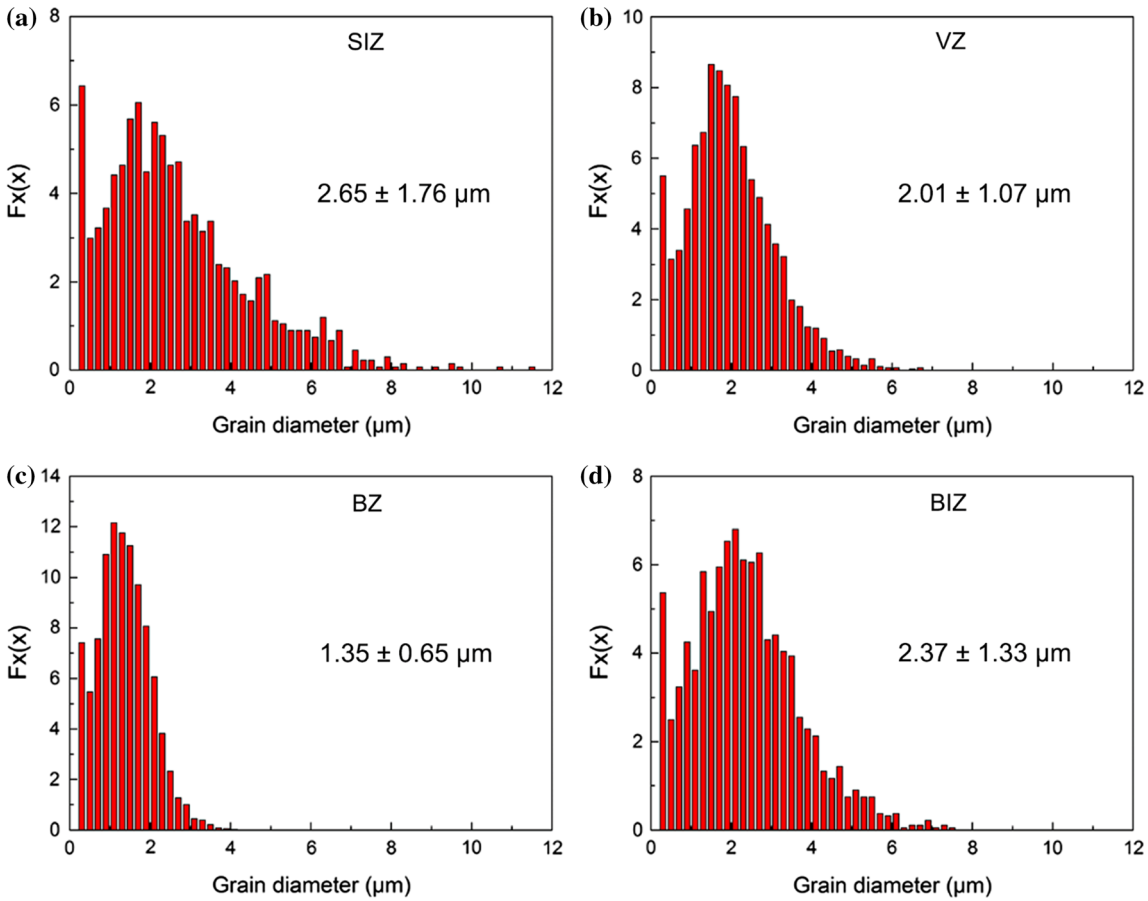

Figure 12 Distribution maps of grain size: **a** SIZ, **b** VZ, **c** BZ and **d** BIZ.

corrosion severity (the size and number of corrosion pits) of different areas in the SZ, the order of corrosion severity can be obtained: BIZ > SIZ > VZ > BZ. This difference between the corrosion severities acquired for each zone can be attributed to the different mixing degree of material flow.

Since SEM and OM are unable to provide the quantitative information about the surface roughness of these corroded samples. As a consequence, AFM was employed to further study about the surface corrosion morphology. As exhibited in Fig. 18, it is concluded that the surface roughness of the four regions in the SZ is slightly larger than that of the BMs (Table 5), indicating lower corrosion resistance presents in the SZ. Moreover, the different regions in the SZ exhibit disparate corrosion morphologies. Both SIZ and BIZ display clearly stepped morphology since their interface line on both sides comes from the two kinds of BMs with different corrosion resistances. The VZ is characterized by an undulating pattern, which is attributed to the layered structure of onion ring formed in the VZ during FSW (Fig. 2c). The surface profile of the BZ is fairly flat due to sufficient mixing resulting in uniform corrosion throughout the BZ. It can be concluded that the sequence of surface roughness in the four regions is: BIZ > SIZ > VZ > BZ, which reveals that uneven corrosion presents in the BIZ, while the corrosion in the BZ is uniform.

Corrosion rate

Corrosion rate of the two BMs and the four regions in the SZ is evaluated based on mass loss measurements of the samples in 3.5 wt% NaCl solution after 336 h. As delineated in Fig. 19, it is obvious that the corrosion rate of the SZ is higher than that of the two BMs. The corrosion rate of the four regions in the SZ decreases in the following order: BIZ > SIZ > VZ > BZ, which is consistent with the results of the corrosion severity (Fig. 17) and surface roughness (Fig. 18 and Table 5). This is associated with the mixing

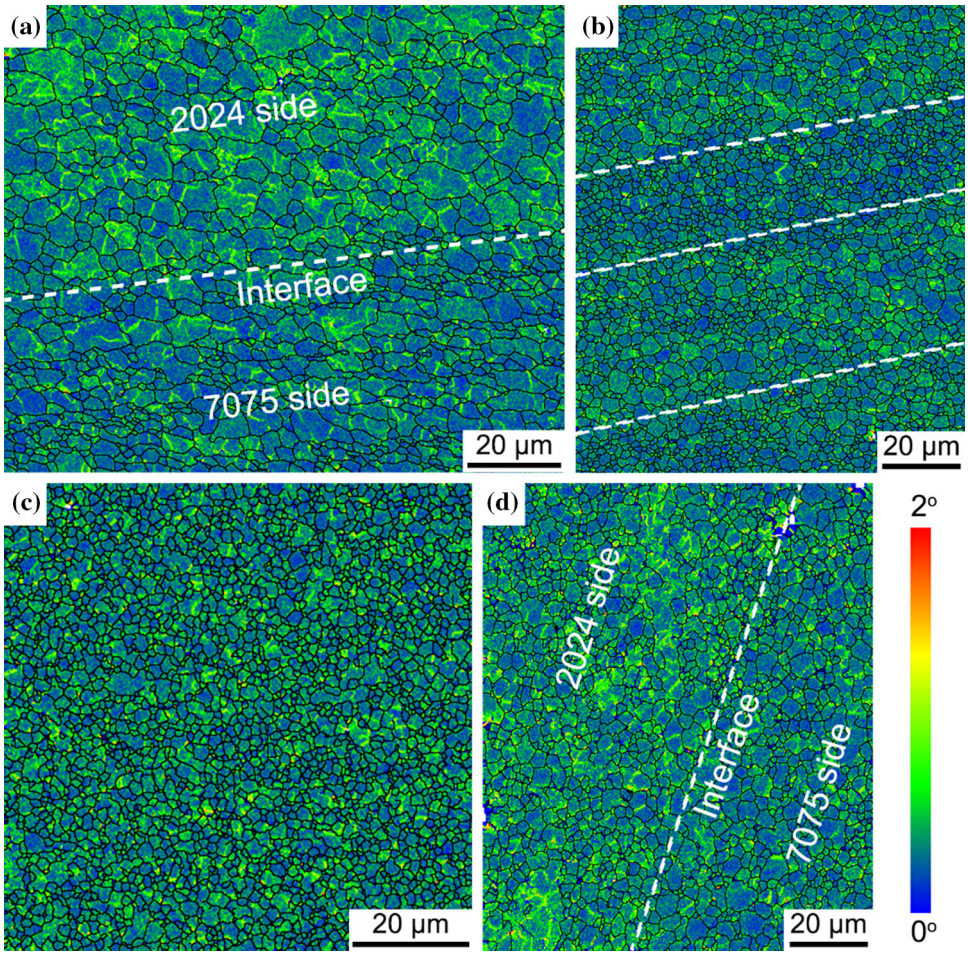

Figure 13 Local misorientation maps of **a** SIZ, **b** VZ, **c** BZ and **d** BIZ.

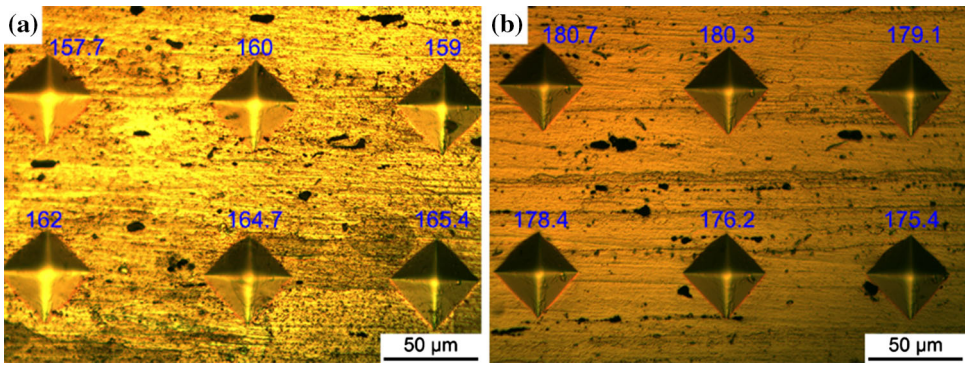

Figure 14 OM images of hardness indentation in the two BMs: **a** AA2024 and **b** AA7075.

degree of materials in different regions of the NZ during FSW.

Electrochemical measurements

Potentiodynamic polarization (PDP) curves

Figure 20 exhibits polarization curves of the specimens in 3.5 wt% NaCl solution. All specimens are not subjected to passivation within the scan potential range. It can be observed that the anodic and cathodic branches of these polarization curves in Fig. 20 are not symmetrical. The cathodic kinetics appear to be very similar in all the specimens. This is because slow diffusion rate of the reactant or reaction produced near the cathode causes concentration polarization during the polarization testing of each specimen, which results in the formation of cathode

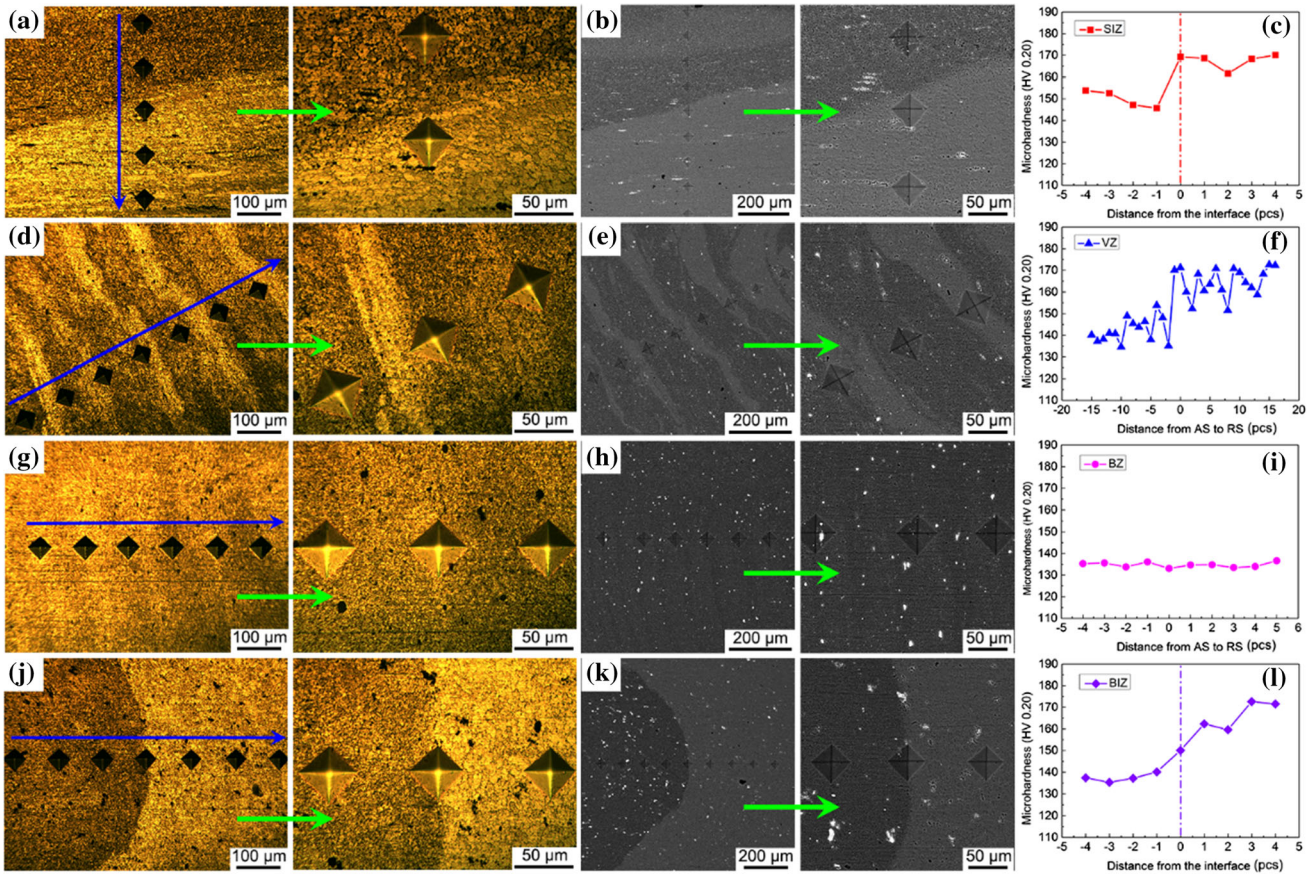

Figure 15 OM micrographs, BSE images and the hardness profile corresponding to the hardness indentation signs **a**–**c** SIZ, **d**–**f** VZ, **g**–**i** BZ and **j**–**l** BIZ.

polarization. The corrosion potentials (E_{corr}) and corrosion current density (I_{corr}) were calculated from the potentiodynamic curves in Fig. 20, as presented in Table 6. It can be found that the E_{corr} of AA7075 is lower than that of AA2024, while higher I_{corr} is presented in the AA7075 compared to the AA2024. More negative value of corrosion potential can be observed in the SIZ and BIZ compared to the VZ and BZ, showing less corrosion resistance. Compared to the magnitude of the E_{corr} values of the four regions in the SZ, their I_{corr} values present an apparent difference. In general, the I_{corr} can be employed to evaluate the active dissolution ability of materials [66]. Table 6 shows that the I_{corr} of SIZ and BIZ is at least about 30 and 50 μA cm^{-2} higher than those of the VZ and BZ, respectively. Thus, it can be concluded that severe corrosion occurs in the SIZ and BIZ.

Electrochemical impedance spectroscopy (EIS) tests

As a most reliable nondestructive electrochemical testing technique, EIS technique can provide more information (e.g., the capacitive characteristic of the materials to be measured) compared with the PDP test [67]. Based on the frequency range, loops formed in Nyquist plot are sorted and the number of loops reveals the number of time constants. High-frequency loop is caused by the electric double layer capacitance between the oxide film on the surface of alloy and the solution, which can be termed as capacitive loop. Intermediate-frequency loop is ascribed to the relaxation process into the oxide film. The appearance of low-frequency inductive reactance arc indicates the occurrence of local corrosion on the surface of alloy [68]. The representative Nyquist and Bode plots obtained from the EIS data are shown in Fig. 21. Nyquist plot in Fig. 21a demonstrates that impedance changes with frequency at certain points and the electrochemical impedance spectrum consists of a

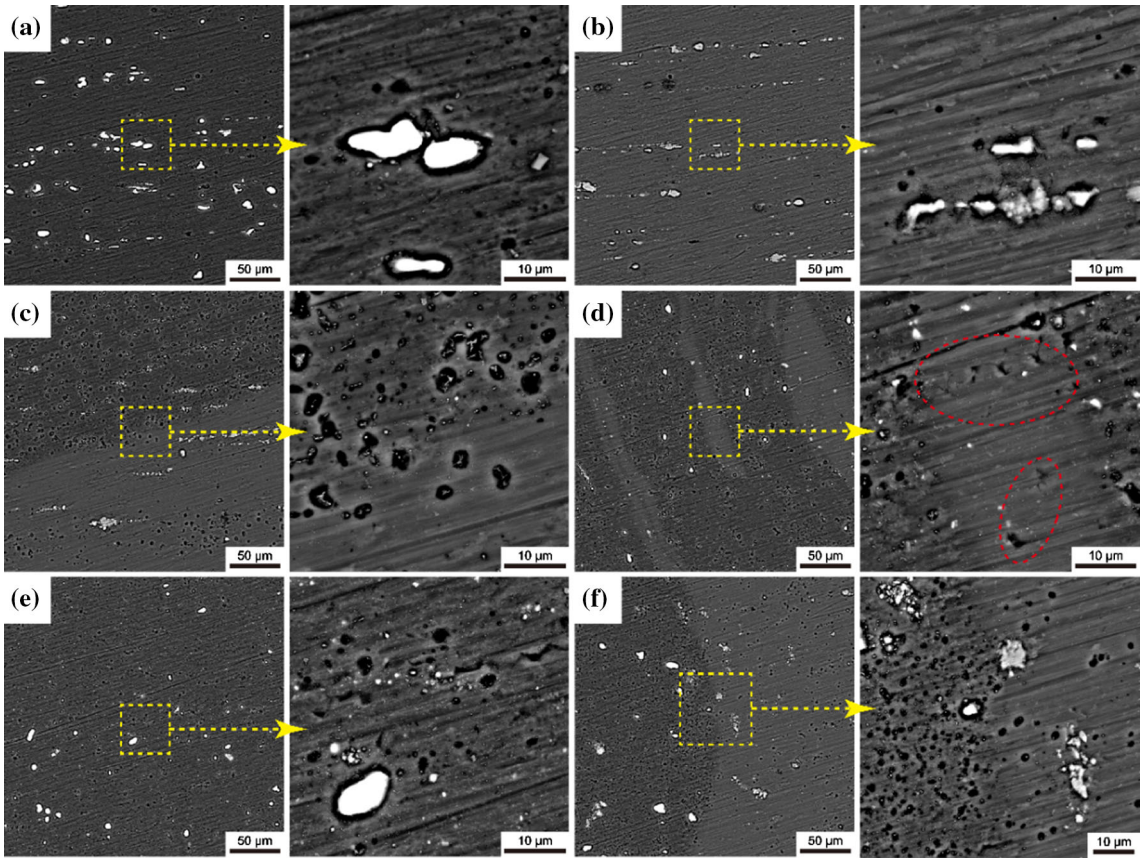

Figure 16 BSE images of the samples immersed in 3.5 wt% NaCl solution for 12 h **a** 2024 BM, **b** 7075 BM, **c** SIZ, **d** VZ, **e** BZ and **f** BIZ.

compressed high-frequency capacitive reactance arc and a low-frequency inductive reactance arc. The former can be mostly attributed to the surface roughness caused by corrosion process, while the latter is generated by the decrease in the protective effect of the oxide film. Besides, the larger diameter of the loop displays the higher impedance and hence reveals the higher corrosion resistance. The phase angle in the Bode plots can reflect the capacitive characteristics of charge accumulation at the interface rather than charge transfer [69]. It can be observed that the maximum phase angle of the BZ is higher than that of other zones in the SZ, suggesting that more passivation layers are formed in the BZ, which is effective to prevent and/or delay corrosion.

Figure 21b, c shows the Bode plots and phase angle diagrams of impedance along with frequency, respectively. Clearly, the impedance and phase angle values of AA2024 are higher than those of AA7075 and the four regions in the SZ almost in the low- and medium-frequency spectra, respectively. Local surface defects are usually recognized in the high-frequency spectrum, while the low- and intermediate-frequency spectra can be used to detect the processes within the film and at the interface of metal/film [70]. Since the ideal phase angle values would be close to 90°, the deviation from the ideal capacitive behavior exists in every response. It is essential to use a constant phase element (CPE) to prove this deviation from the ideal state. The CPE behavior can be ascribed to the surface roughness, impurities, grain boundaries, species adsorption and formation of porous layers [71]. Theoretically, the impedance of CPE is expressed as follows [37]:

$$Z_{\mathrm{CPE}} = \frac{1}{Q(jw)^{\alpha}} \tag{5}$$

where Q, j, ω and α are the CPE constant, the imaginary number ($j^2 = 1$), the angular frequency in rad/s and the CPE exponent, respectively. Here, what can be represented by a CPE is determined by α: a resistant ($\alpha = 0$, $Z_0 = R$), a capacitance ($\alpha = 1$, $Z_0 = C$) or a Warbug impedance ($\alpha = 0.5$, $Z_0 = W$).

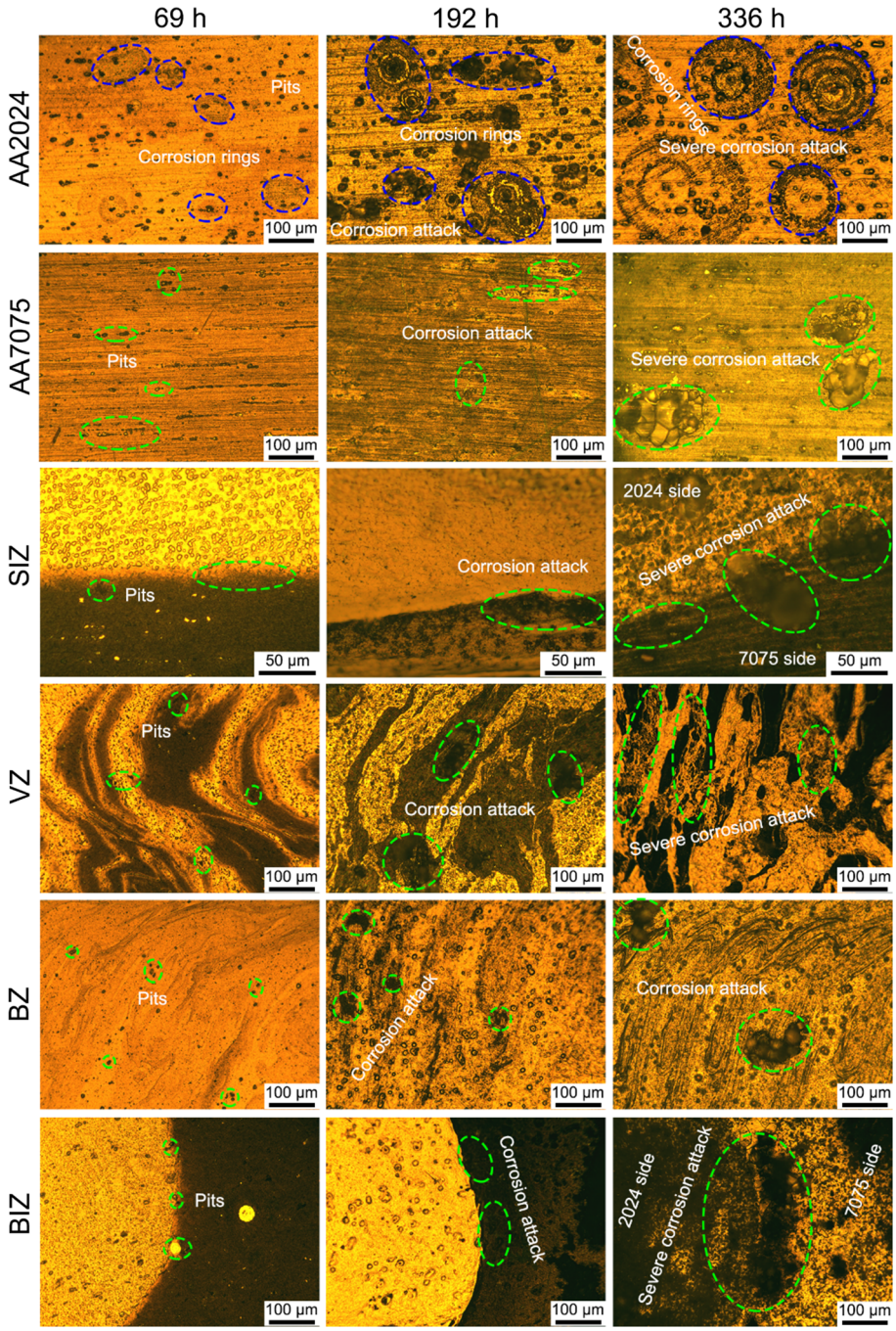

Figure 17 OM images of the samples immersed in 3.5 wt% NaCl solution after 69 h, 192 h and 336 h.

The fitted EIS data from the equivalent circuit (Fig. 21d) are exhibited in Table 7, where R_S and R_P are the solution resistance and the polarization resistance, respectively. Y_O is the channel which turns into inductor, resistor or capacitor at $n = -1, 0$ or 1, respectively. L and R_L are the electrical inductance and the corresponding inductive impedance, respectively. All the Chi-squared values of below 0.01 in Table 7 illustrate good fitting results. Due to the deviation of the capacitance of the circuit from the ideal capacitor, the n value less than 1 indicates the characteristic behavior of the capacitor of an oxide film. As given in Table 7, the R_S of all the specimens is almost the same, which can be neglected compared with the R_P. The R_P value of the four regions in the SZ increases in the sequence of BIZ, SIZ, VZ and BZ. In general, the Rp is believed to be inversely proportional to the corrosion rate; thus, it can be used to

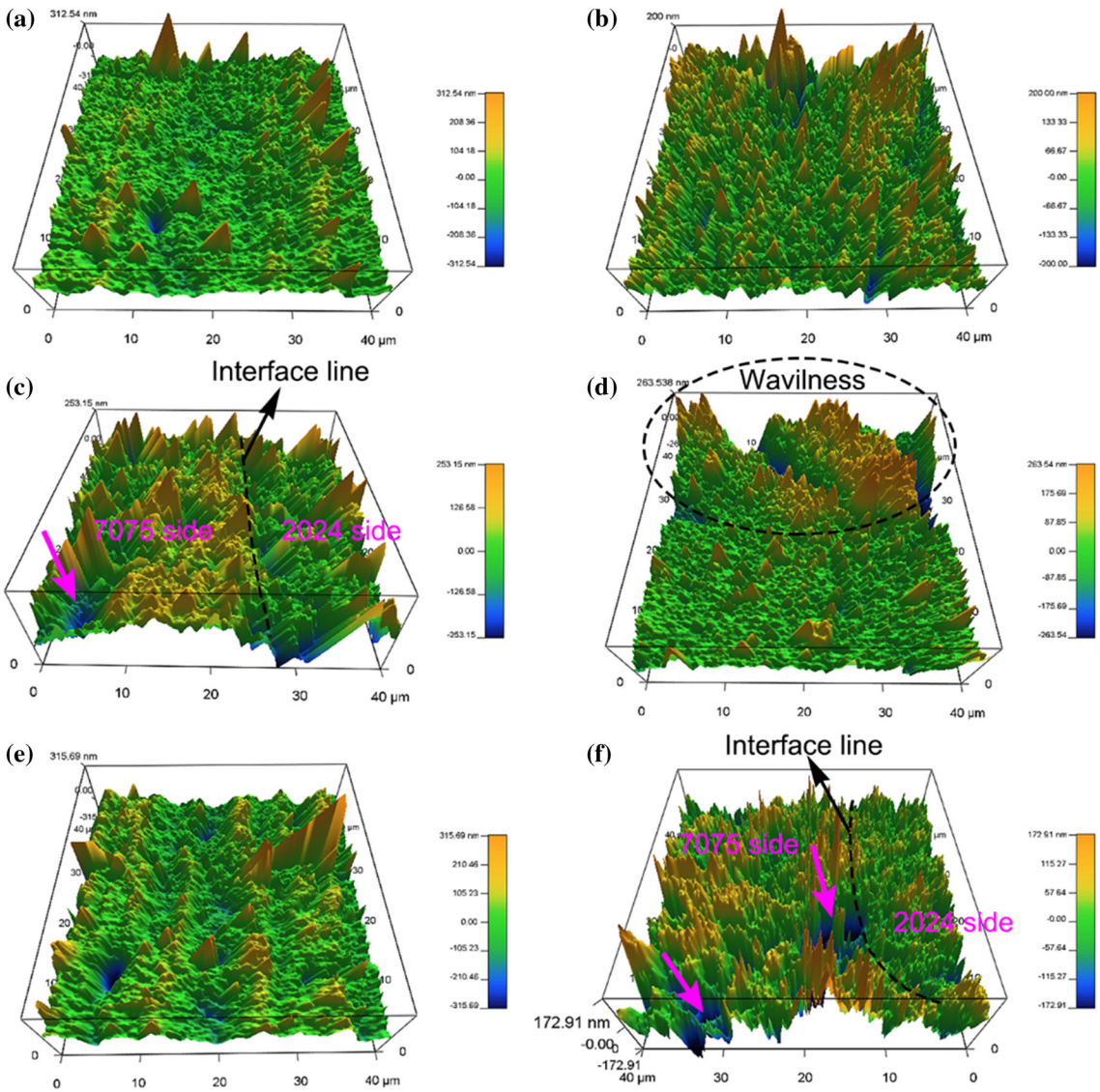

Figure 18 AFM micrographs of the samples in 3.5 wt% NaCl solution after 69 h **a** 2024 BM, **b** 7075 BM, **c** SIZ, **d** VZ, **e** BZ and **f** BIZ.

Table 5 Surface roughness of the BMs and the four regions in the SZ in 3.5 wt% NaCl solution after 69 h

Samples	AA2024	AA7075	SIZ	VZ	BZ	BIZ
Ra (nm)	37.46 ± 2.83	41.31 ± 3.36	51.72 ± 4.83	46.76 ± 3.46	42.01 ± 5.05	53.75 ± 4.81

assess the corrosion resistance of alloys [72]. Apparently, the R_P of BIZ and SIZ shows the worse corrosion performance when compared with other samples. Thus, it can be concluded that the sequence of corrosion resistance within different regions of the SZ is: BZ > VZ > SIZ > BIZ.

Corrosion mechanism analysis

The corrosion behavior of aluminum alloys is mainly affected by some microstructural factors, such as grain size and the precipitation particles types. On the basis of Gollapudi [58], the effect of grain size distribution on corrosion behavior depends on the average grain size and the standard deviation of

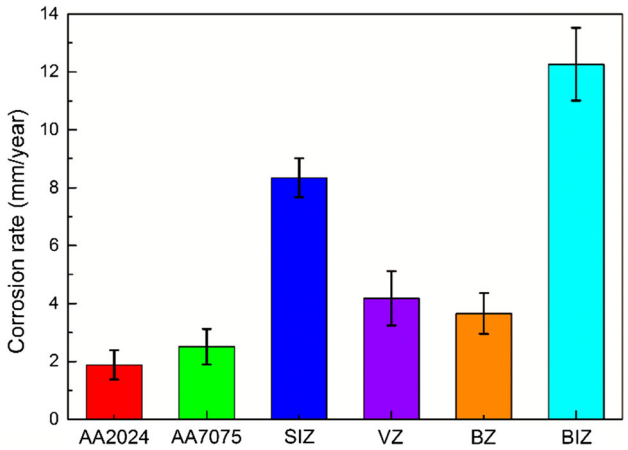

Figure 19 Corrosion rate of the samples in 3.5 wt% NaCl solution after 336 h.

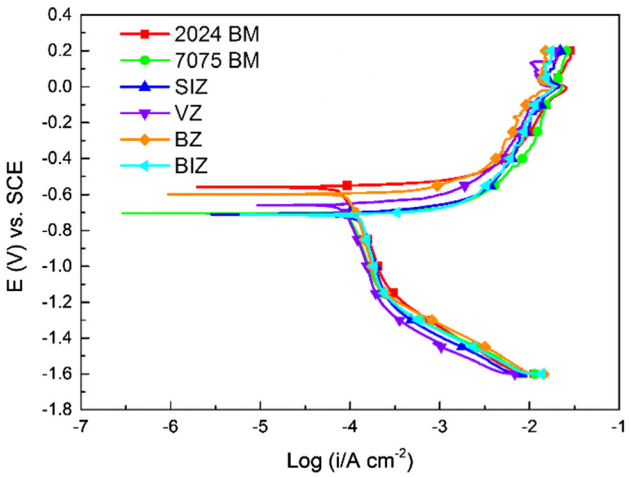

Figure 20 PDP curves of the samples in 3.5 wt% NaCl solution.

Table 6 Polarization parameters of the BMs and the four regions in the SZ

Specimens	E_{corr} (V_{SCE})	I_{corr} (μA cm^{-2})
2024 BM	− 0.557 ± 0.106	71.5 ± 7.526
7075 BM	− 0.704 ± 0.087	90.2 ± 5.498
SIZ	− 0.709 ± 0.005	119.23 ± 5.055
VZ	− 0.601 ± 0.069	98.57 ± 6.749
BZ	− 0.597 ± 0.004	93.77 ± 6.167
BIZ	− 0.711 ± 0.013	131.99 ± 5.749

grain size. Gollapudi reported that the function of the above two factors is imperative when the average grain size is below 100 nm, but not significant when the size is larger than 1 μm. Figure 11 shows that a large number of fine grains are produced in the SZ. The statistical results in Fig. 12 indicate that the average grain size of SIZ, VZ, BZ and BIZ exceeds 1 μm. Thus, we can summarize that the grain size has little influence on the corrosion behavior of the SZ.

After immersion for 12 h (Fig. 16), plenty of pits can be detected on the AA2024 side and in these regions near the interface on both sides due to the formation of Cu-rich particles (Fig. 4 and Table 2, Fig. 8 and Table 3, Fig. 9 and Table 4 and Fig. 10). The pitting process is portrayed in Fig. 22. The corrosion potential of Al matrix is more negative than that of the Cu-rich particles [73], which results in the dissolution of Al matrix around these particles in corrosive environments containing chloride ions. With the prolonged immersion time up to 69 h, the corrosion morphologies of both SIZ and BIZ present distinct step shape on both sides of the interface line (Fig. 18). Interestingly, the horizontal height of 2024 side is lower than that of 7075 side in the SIZ and BIZ, which is related to the distribution of the stored energy. Zhang et al. [59] and Ma et al. [74] found that the grains with higher stored energy are liable to dissolve or corrode. Figure 13 shows that the stored energy distribution of AA2024 side at the interface is more intensive and concentrated than that of AA7075 side. Consequently, the corrosion is prone and sensitive to occur on 2024 side at the interface. Besides, it is also found that the deeper pits are formed locally on AA7075 side (marked by the pink arrows in Fig. 18c, f). This is because the chemical composition of AA7075 side is dominated by Mg and Zn elements and the particles containing Mg and Zn elements are preferentially dissolved due to their high reactivity as anode [35].

During FSW, different microstructural regions can be produced. Thus, the zonal inhomogeneity is more evident and causes local galvanic corrosion especially for the welding of the dissimilar aluminum alloys [34–36]. A necessary condition for galvanic corrosion is a large potential difference between two metals. The formation condition for galvanic corrosion is a potential difference of 50 mV or more between two metals in contact [75]. According to the PDP results in Fig. 20 and Table 6, the potential difference of the two BMs is about 147 mV, indicating the formation of galvanic corrosion at the interface of the SZ. In this work, we have proposed that the order of mixing degree of materials flow in the NZ is: BZ > VZ > SIZ > BIZ (Figs. 2, 5 and 6), which is consistent with the sequence of corrosion resistance (Fig. 21 and

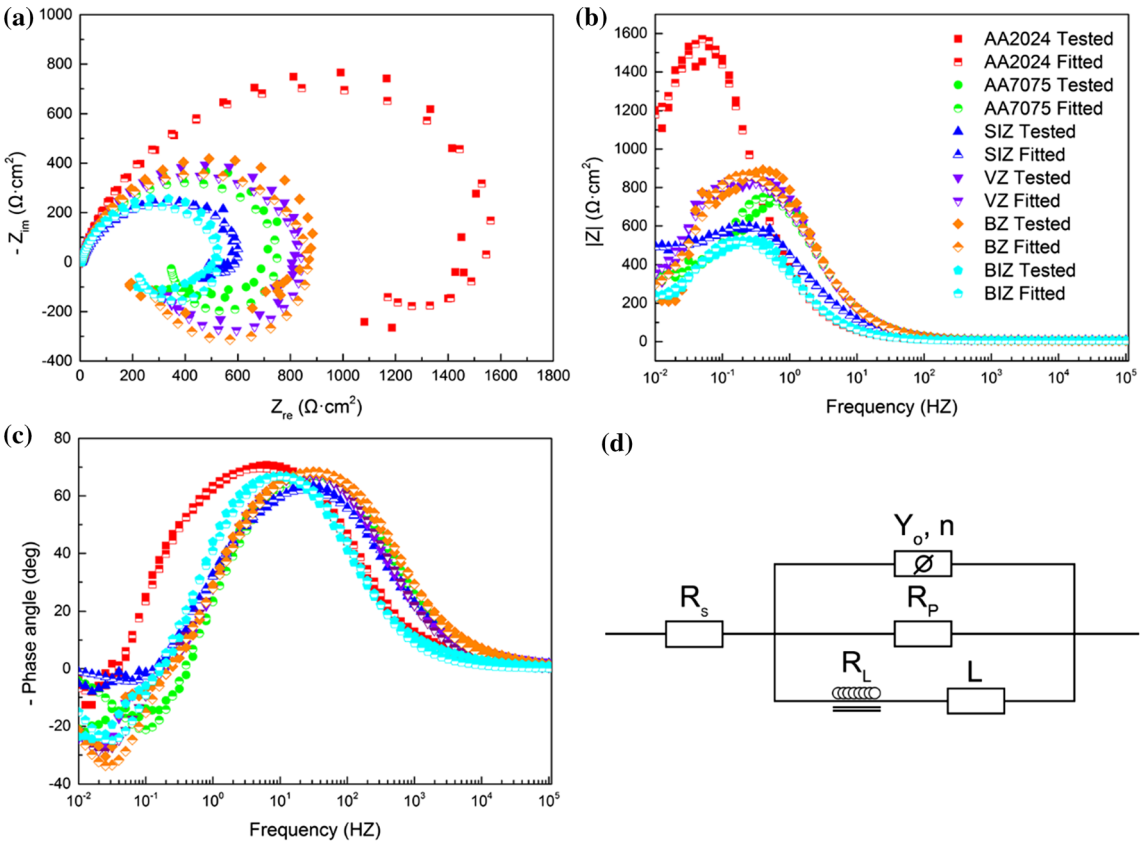

Figure 21 EIS test results of the samples in 3.5 wt% NaCl solution: **a** Nyquist plot, **b** Bode plot, **c** phase plot and **d** equivalent circuit for fitting the EIS data.

Table 7 Fitted EIS parameters from the equivalent circuit model in Fig. 21c

Samples	R_S (Ω cm^2)	Y_O (Ω^{-1} cm^{-2} s^n)	n	R_P (Ω cm^2)	L (H cm^{-2})	R_L (Ω cm^2)	Chi-square
2024 BM	5.49	5.314×10^{-4}	0.84	1868	2.178×10^{4}	266	3.296×10^{-3}
7075 BM	6.58	1.577×10^{-4}	0.85	827.3	1.254×10^{3}	576	7.888×10^{-3}
SIZ	5.85	3.039×10^{-4}	0.80	676.5	3.491×10^{3}	371.3	1.961×10^{-3}
VZ	7.38	1.544×10^{-4}	0.86	870.5	5.126×10^{3}	435.4	5.664×10^{-3}
BZ	5.52	1.539×10^{-4}	0.85	906.1	3.622×10^{3}	338.6	2.130×10^{-3}
BIZ	6.82	4.088×10^{-4}	0.88	555.6	2.597×10^{3}	328.4	6.540×10^{-3}

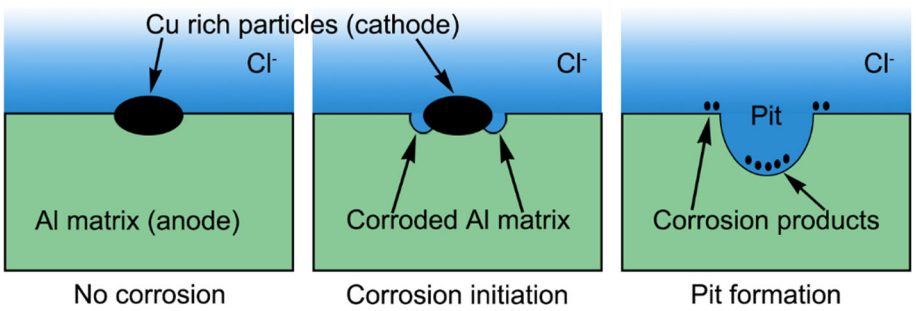

Figure 22 Schematic of various stages in the pitting process.

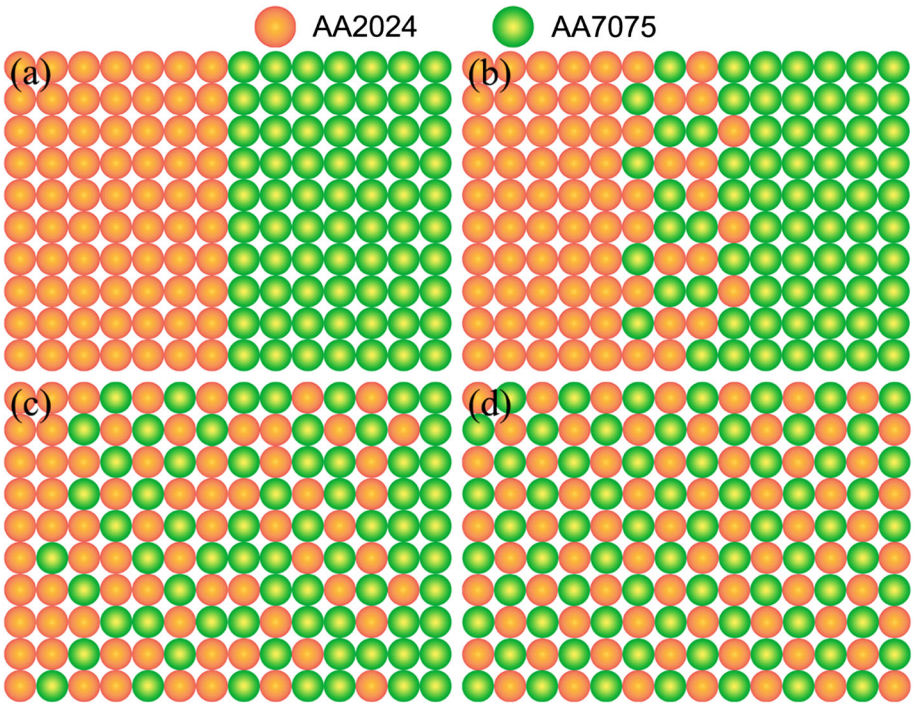

Figure 23 Schematics of varying mixing degrees in the two BMs: **a** no mixing, **b** slight mixing or diffusion, **c** relatively uniform mixing and **d** thorough mixing.

Table 7). It can be concluded that different mixing degrees show various corrosion performance. Although slight mixing or diffusion behavior occurs in the SIZ and BIZ, a strong galvanic corrosion is still present. Further, the corrosion resistance of both BZ and VZ is significantly higher than that of SIZ and BIZ (Fig. 21 and Table 7), which demonstrates that sufficient material mixing can weaken the galvanic corrosion.

The effect of material mixing degree on galvanic corrosion can be expounded by the schematic diagram in Fig. 23. As shown in Fig. 23a, without mixing of the two materials, obvious galvanic corrosion can be generated. With the two materials being slightly mixed (Fig. 23b), the elements at the interface migrate and diffuse lightly each other, corresponding to the SIZ and BIZ; at this time, the galvanic corrosion still exists, indicating that slight element diffusion has little effect on galvanic corrosion (Fig. 21 and Table 7). When the two materials are completely mixed (Fig. 23d), it can be considered to form a new material. In this case, the corrosion potential difference is close to 0 or there is no potential difference. Thus, relatively uniform mixing of materials (Fig. 23c), corresponds to the BZ, can significantly weaken galvanic corrosion and then can result in higher corrosion resistance (Fig. 21 and Table 7). The results of immersion test (Fig. 17) and corrosion rate (Fig. 19) also confirm this behavior.

In addition, as displayed in Fig. 17, more severe corrosion occurs near the borderline, and the areas away from the borderline are less corrosive, which is similar to the results of Won et al. [76]. Corrosion is caused by electrochemical reaction, which involves charge transfer process. Since metal is a good conductor, electron transport in the metal is not a problem when limiting the distance corrosion occurs. The ionic transport rate in electrolyte is not fast enough as the electron transport. Hence, its resistance would be increased with the distance away from the borderline in the effective distance, leading to the weak corrosion. As a consequence, severe corrosion occurs near the interface area due to the action of galvanic corrosion, while relatively light corrosion can be found in the regions away from the interface.

Conclusions

A thorough study on the localized corrosion behavior in the SZ of the dissimilar FSW AA2024-7075 joint has been implemented. Some significant conclusions can be drawn from this work as follows:

1. The sequence of mixing degree of materials in the four regions of the SZ is: BZ > VZ > SIZ > BIZ,

which is in contrast to the order of corrosion rate and surface roughness, indicating that mixing degree of materials significantly affects the corrosion properties.

2. Immersion test, potentiodynamic polarization test and EIS test results indicate that galvanic corrosion occurs in the SIZ and BIZ, resulting in higher corrosion rate and lower corrosion resistance. Lower corrosion rate and higher corrosion resistance are found in the BZ due to sufficient material mixing obviously weakening the galvanic corrosion. The corrosion resistance of VZ is between that of BZ and SIZ because material mixing results in the mutual diffusion of the elements and then cripples the effect of galvanic couplings.
3. Plentiful of Cu-rich constituent particles are formed on the AA2024 side and the areas near the interface on both sides, and corrosion originates from these regions.
4. Grain size has little influence on corrosion behavior of the SZ, while the local regions with higher stored energy in the SZ are more sensitive and liable to corrosion.
5. Conspicuous element diffusion behavior occurs at the interface region, especially Cu and Zn, which causes a gradient distribution of hardness values at the interface.
6. A distance effect can be found in galvanic corrosion; for example, serious corrosion occurs at the interface, while light corrosion presents in the regions away from the interface.

Acknowledgements

We greatly acknowledge the financial support of the "National Natural Science Foundation of China" (No. 51421001) and "Fundamental Research Funds for the Central Universities" (No. 2018CDJDCL0019). We also acknowledge the Electron Microscopy Center of Chongqing University for providing SEM and TEM test channel.

References

[1] Dursun T, Soutis C (2014) Recent developments in advanced aircraft aluminium alloys. Mater Des 56:862–871

[2] Rioja RJ, Liu J (2012) The evolution of Al-Li base products for aerospace and space applications. Metall Mater Trans A 43:3325–3337

[3] Texier D, Atmani F, Bocher P, Nadeau F, Chen J, Zedan Y et al (2018) Fatigue performances of FSW and GMAW aluminum alloys welded joints: competition between microstructural and structural-contact-fretting crack initiation. Int J Fatigue 116:220–233

[4] Wang G, Zhao Y, Hao Y (2018) Friction stir welding of high-strength aerospace aluminum alloy and application in rocket tank manufacturing. J Mater Sci Technol 34:73–91

[5] Padhy G, Wu C, Gao S (2018) Friction stir based welding and processing technologies-processes, parameters, microstructures and applications: a review. J Mater Sci Technol 34:1–38

[6] Kartsonakis I, Dragatogiannis D, Koumoulos E, Karantonis A, Charitidis C (2016) Corrosion behaviour of dissimilar friction stir welded aluminium alloys reinforced with nanoadditives. Mater Des 102:56–67

[7] Zhang C, Huang G, Cao Y, Zhu Y, Liu Q (2019) On the microstructure and mechanical properties of similar and dissimilar AA7075 and AA2024 friction stir welding joints: effect of rotational speed. J Manuf Process 37:470–487

[8] Khan NZ, Siddiquee AN, Khan ZA, Mukhopadhyay AK (2017) Mechanical and microstructural behavior of friction stir welded similar and dissimilar sheets of AA2219 and AA7475 aluminium alloys. J Alloys Compd 695:2902–2908

[9] Tang J, Shen Y (2016) Numerical simulation and experimental investigation of friction stir lap welding between aluminum alloys AA2024 and AA7075. J Alloys Compd 666:493–500

[10] Mishra RS, Ma Z (2005) Friction stir welding and processing. Mater Sci Eng R 50:1–78

[11] Nandan R, DebRoy T, Bhadeshia H (2008) Recent advances in friction-stir welding–process, weldment structure and properties. Prog Mater Sci 53:980–1023

[12] Donatus U, Thompson G, Zhou X, Wang J, Cassell A, Beamish K (2015) Corrosion susceptibility of dissimilar friction stir welds of AA5083 and AA6082 alloys. Mater Charact 107:85–97

[13] Li X, Li J, Liao Z, Jin F, Zhang F, Xiong J (2016) Asymmetric microstructure and fracture behaviour of friction stir welded joints of 2024 aluminium alloy under cyclical load. Sci Technol Weld Join 21:515–522

[14] Sahu PK, Pal S (2017) Mechanical properties of dissimilar thickness aluminium alloy weld by single/double pass FSW. J Mater Process Technol 243:442–455

[15] Sharghi E, Farzadi A (2018) Simulation of strain rate, material flow, and nugget shape during dissimilar friction stir

welding of AA6061 aluminum alloy and Al-Mg_2Si composite. J Alloys Compd 748:953–960

[16] Chenghang Z, Guangjie H, Yu C, Wei L, Qing L (2019) EBSD analysis of nugget zone in dissimilar friction stir welded AA2024-AA7075 joint along weld thickness. Rare Metal Mat Eng 48:3161–3166

[17] Zhang C, Huang G, Cao Y, Zhu Y, Huang X, Zhou Y et al (2020) Microstructure evolution of thermo-mechanically affected zone in dissimilar AA2024/7075 joint produced by friction stir welding. Vacuum 179:109515

[18] Threadgill P, Leonard A, Shercliff H, Withers P (2009) Friction stir welding of aluminium alloys. Int Mater Rev 54:49–93

[19] Zhang C, Cui L, Wang D, Liu Y, Liu C, Li H (2019) The heterogeneous microstructure of heat affect zone and its effect on creep resistance for friction stir joints on 9Cr–1.5 W heat resistant steel. Scr Mater 158:6–10

[20] Zhang C, Cao Y, Huang G, Zeng Q, Zhu Y, Huang X et al (2020) Influence of tool rotational speed on local microstructure, mechanical and corrosion behavior of dissimilar AA2024/7075 joints fabricated by friction stir welding. J Manuf Process 49:214–226

[21] Paglia C, Jata K, Buchheit R (2006) A cast 7050 friction stir weld with scandium: microstructure, corrosion and environmental assisted cracking. Mater Sci Eng A 424:196–204

[22] Paglia C, Buchheit R (2008) A look in the corrosion of aluminum alloy friction stir welds. Scr Mater 58:383–387

[23] Lumsden J, Mahoney M, Rhodes C, Pollock G (2003) Corrosion behavior of friction-stir-welded AA7050-T7651. Corrosion 59:212–219

[24] Bousquet E, Poulon-Quintin A, Puiggali M, Devos O, Touzet M (2011) Relationship between microstructure, microhardness and corrosion sensitivity of an AA 2024-T3 friction stir welded joint. Corros Sci 53:3026–3034

[25] Paglia C, Buchheit R (2008) The time–temperature–corrosion susceptibility in a 7050-T7451 friction stir weld. Mater Sci Eng, A 492:250–254

[26] Kang J, Fu R-d, Luan G-h, Dong C-l, He M (2010) In-situ investigation on the pitting corrosion behavior of friction stir welded joint of AA2024-T3 aluminium alloy. Corros Sci 52:620–626

[27] Strass B, Wagner G, Conrad C, Wolter B, Benfer S, Fuerbeth W (2014) Realization of Al/Mg-hybrid-joints by ultrasound supported friction stir welding-mechanical properties, microstructure and corrosion behavior. Adv Mater Res Trans Tech Publ 966–967:521–535

[28] Akinlabi ET, Andrews A, Akinlabi SA (2014) Effects of processing parameters on corrosion properties of dissimilar friction stir welds of aluminium and copper. Trans Nonferr Metal Soc 24:1323–1330

[29] Sarvghad-Moghaddam M, Parvizi R, Davoodi A, Haddad-Sabzevar M, Imani A (2014) Establishing a correlation between interfacial microstructures and corrosion initiation sites in Al/Cu joints by SEM–EDS and AFM–SKPFM. Corros Sci 79:148–158

[30] Rajani HZ, Esmaeili A, Mohammadi M, Sharbati M, Givi M (2012) The role of metal-matrix composite development during friction stir welding of aluminum to brass in weld characteristics. J Mater Eng Perform 21:2429–2437

[31] Seo B, Song KH, Park K (2018) Corrosion properties of dissimilar friction stir welded 6061 aluminum and HT590 steel. Met Mater Int 24:1232–1240

[32] Larson D, Waldera B, Sitter C, Kalita S (2011) Microstructure and corrosion investigation of friction stir welds of dissimilar aluminum alloys. Mater Sci Technol Conf Exhib 12:1546–1553

[33] Shen C, Zhang J, Ge J (2011) Microstructures and electrochemical behaviors of the friction stir welding dissimilar weld. J Environ Sci 23:S32–S35

[34] Bertoncello JC, Manhabosco SM, Dick LF (2015) Corrosion study of the friction stir lap joint of AA7050-T76511 on AA2024-T3 using the scanning vibrating electrode technique. Corros Sci 94:359–367

[35] De Abreu CP, Costa I, De Melo HG, Pébère N, Tribollet B, Vivier V (2017) Multiscale Electrochemical Study of Welded Al Alloys Joined by Friction Stir Welding. J Electrochem Soc 164:C735–C746

[36] Davoodi A, Esfahani Z, Sarvghad M (2016) Microstructure and corrosion characterization of the interfacial region in dissimilar friction stir welded AA5083 to AA7023. Corros Sci 107:133–144

[37] Fattah-alhosseini A, Naseri M, Gholami D, Imantalab O, Attarzadeh F, Keshavarz M (2019) Microstructure and corrosion characterization of the nugget region in dissimilar friction-stir-welded AA5083 and AA1050. J Mater Sci 54:777–790. https://doi.org/10.1007/s10853-018-2820-4

[38] Zhao Z, Liang H, Zhao Y, Yan K (2018) Effect of exchanging advancing and retreating side materials on mechanical properties and electrochemical corrosion resistance of Dissimilar 6013-T4 and 7003 aluminum alloys FSW joints. J Mater Eng Perform 27:1777–1783

[39] Wu P, Deng Y, Fan S, Ji H, Zhang X (2018) A study on dissimilar friction stir welded between the Al–Li–Cu and the Al–Zn–Mg–Cu alloys. Materials 11:1132

[40] Bocchi S, Cabrini M, D'Urso G, Giardini C, Lorenzi S, Pastore T (2018) The influence of process parameters on mechanical properties and corrosion behavior of friction stir welded aluminum joints. J Manuf Process 35:1–15

[41] Niu P, Li W, Li N, Xu Y, Chen D (2019) Exfoliation corrosion of friction stir welded dissimilar 2024-to-7075 aluminum alloys. Mater Charact 147:93–100

[42] Zhang C, Huang G, Cao Y, Wu X, Huang X, Liu Q (2019) Optimization of Tensile and Corrosion Properties of Dissimilar Friction Stir Welded AA2024-7075 Joints. J Mater Eng Perform 28:183–199

[43] Galvão I, Leal R, Rodrigues D, Loureiro A (2013) Influence of tool shoulder geometry on properties of friction stir welds in thin copper sheets. J Mater Process Technol 213:129–135

[44] Zhang C, Huang G, Cao Y, Zhu Y, Li W, Wang X et al (2019) Microstructure and mechanical properties of dissimilar friction stir welded AA2024-7075 joints: Influence of joining material direction. Mater Sci Eng A 766:138368

[45] Sutton MA, Yang B, Reynolds AP, Yan J (2004) Banded microstructure in 2024-T351 and 2524-T351 aluminum friction stir welds: part II. Mechanical characterization. Mater Sci Eng A 364:66–74

[46] Tongne A, Desrayaud C, Jahazi M, Feulvarch E (2017) On material flow in friction stir welded Al alloys. J Mater Process Technol 239:284–296

[47] Buchheit R, Grant R, Hlava P, McKenzie B, Zender G (1997) Local dissolution phenomena associated with S phase (Al_2CuMg) particles in aluminum alloy 2024-T3. J Electrochem Soc 144:2621–2628

[48] Dziallach S, Bleck W, Köhler M, Nicolini G, Richter S (2009) Roll-bonded titanium/stainless-steel couples, part 1: diffusion and interface-layer investigations. Adv Eng Mater 11:75–81

[49] Martinez N, Kumar N, Mishra R, Doherty K (2017) Microstructural variation due to heat gradient of a thick friction stir welded aluminum 7449 alloy. J Alloys Compd 713:51–63

[50] Sha G, Marceau R, Gao X, Muddle B, Ringer S (2011) Nanostructure of aluminium alloy 2024: segregation, clustering and precipitation processes. Acta Mater 59:1659–1670

[51] Wang S, Starink M (2005) Precipitates and intermetallic phases in precipitation hardening Al–Cu–Mg–(Li) based alloys. Int Mater Rev 50:193–215

[52] Ghosh A, Ghosh M, Shankar G (2018) On the role of precipitates in controlling microstructure and mechanical properties of Ag and Sn added 7075 alloys during artificial ageing. Mater Sci Eng A 738:399–411

[53] Wolverton C (2001) Crystal structure and stability of complex precipitate phases in Al–Cu–Mg–(Si) and Al–Zn–Mg alloys. Acta Mater 49:3129–3142

[54] Tanaka T, Nezu M, Uchida S, Hirata T (2020) Mechanism of intermetallic compound formation during the dissimilar friction stir welding of aluminum and steel. J Mater Sci 55:3064–3072. https://doi.org/10.1007/s10853-019-04106-2

[55] Ross K, Reza-E-Rabby M, McDonnell M, Whalen SA (2019) Advances in dissimilar metals joining through temperature control of friction stir welding. MRS Bull 44:613–618

[56] Pereira VF, Fonseca EB, Costa AM, Bettini J, Lopes ES (2020) Nanocrystalline structural layer acts as interfacial bond in Ti/Al dissimilar joints produced by friction stir welding in power control mode. Scr Mater 174:80–86

[57] Gotawala N, Shrivastava A (2019) Investigation of interfacial diffusion during dissimilar friction stir welding. Friction stir welding and processing X. Springer, New York, pp 109–119

[58] Gollapudi S (2012) Grain size distribution effects on the corrosion behaviour of materials. Corros Sci 62:90–94

[59] Zhang X, Zhou X, Hashimoto T, Lindsay J, Ciuca O, Luo C et al (2017) The influence of grain structure on the corrosion behaviour of 2A97-T3 Al-Cu-Li alloy. Corros Sci 116:14–21

[60] Liu Q, Jensen DJ, Hansen N (1998) Effect of grain orientation on deformation structure in cold-rolled polycrystalline aluminium. Acta Mater 46:5819–5838

[61] Calcagnotto M, Ponge D, Demir E, Raabe D (2010) Orientation gradients and geometrically necessary dislocations in ultrafine grained dual-phase steels studied by 2D and 3D EBSD. Mater Sci Eng A 527:2738–2746

[62] Ma Z, Feng A, Chen D, Shen J (2018) Recent advances in friction stir welding/processing of aluminum alloys: microstructural evolution and mechanical properties. Crit Rev Solid State 43:269–333

[63] Cam G, Mistikoglu S (2014) Recent developments in friction stir welding of Al-alloys. J Mater Eng Perform 23:1936–1953

[64] Dimitrov N, Mann J, Sieradzki K (1999) Copper redistribution during corrosion of aluminum alloys. J Electrochem Soc 146:98–102

[65] de Sousa Araujo JV, Donatus U, Queiroz FM, Terada M, Milagre MX, de Alencar MC et al (2018) On the severe localized corrosion susceptibility of the AA2198-T851 alloy. Corros Sci 133:132–140

[66] Meng G, Li Y, Shao Y, Zhang T, Wang Y, Wang F et al (2016) Effect of microstructures on corrosion behavior of nickel coatings:(II) competitive effect of grain size and twins density on corrosion behavior. J Mater Sci Technol 32:465–469

[67] Trdan U, Grum J (2014) SEM/EDS characterization of laser shock peening effect on localized corrosion of Al alloy in a near natural chloride environment. Corros Sci 82:328–338

[68] Sinhmar S, Dwivedi DK (2018) A study on corrosion behavior of friction stir welded and tungsten inert gas welded AA2014 aluminium alloy. Corros Sci 133:25–35

[69] Park S-M, Yoo J-S (2003) Peer reviewed: electrochemical impedance spectroscopy for better electrochemical measurements. ACS Publications, Washington

[70] Nam N, Dai L, Mathesh M, Bian M, Thu V (2016) Role of friction stir welding–traveling speed in enhancing the corrosion resistance of aluminum alloy. Mater Chem Phys 173:7–11

[71] Escrivà-Cerdán C, Blasco-Tamarit E, García-García DM, García-Antón J, Akid R, Walton J (2013) Effect of temperature on passive film formation of UNS N08031 Cr–Ni alloy in phosphoric acid contaminated with different aggressive anions. Electrochim Acta 111:552–561

[72] Wang Z, Chen C, Jiu J, Nagao S, Nogi M, Koga H et al (2017) Electrochemical behavior of Zn-xSn high-temperature solder alloys in 0.5 M NaCl solution. J Alloys Compd 716:231–239

[73] Hu T, Shi H, Hou D, Wei T, Fan S, Liu F et al (2019) A localized approach to study corrosion inhibition of intermetallic phases of AA 2024-T3 by cerium malate. Appl Surf Sci 467:1011–1032

[74] Ma Y, Zhou X, Liao Y, Yi Y, Wu H, Wang Z et al (2016) Localised corrosion in AA 2099-T83 aluminium-lithium alloy: the role of grain orientation. Corros Sci 107:41–48

[75] Schneider M, Kremmer K, Lämmel C, Sempf K, Herrmann M (2014) Galvanic corrosion of metal/ceramic coupling. Corros Sci 80:191–196

[76] Won S, Seo B, Park JM, Kim HK, Song KH, Min S-H et al (2018) Corrosion behaviors of friction welded dissimilar aluminum alloys. Mater Charact 144:652–660

Publisher's Note Springer Nature remains neutral with regard to jurisdictional claims in published maps and institutional affiliations.